The Faintest, Extremely Variable X-ray Tidal Disruption Event from a Supermassive Black Hole Binary?

Mengqiu Huang,^{1,2} Yongquan Xue*,^{1,2} Shuo Li**,³ Fukun Liu,^{4,5} Shifu Zhu,^{1,2} Jin-Hong Chen,⁶ Rong-Feng Shen,^{7,8} Yibo Wang,^{1,2} Yi Yang,^{9,10} Ning Jiang,^{1,2} Franz Erik Bauer,^{11,12,13} Cristian Vignali,^{14,15} Fan Zou,¹⁶ Jialai Wang,^{1,2} Alexei V. Filippenko,¹⁰ Bin Luo,^{17,18} Chen Qin,^{1,2} Jonathan Quirola-Vásquez,¹⁹ Jun-Xian Wang,^{1,2} Lulu Fan,^{1,2} Mouyuan Sun,²⁰ Qingwen Wu,²¹ Qingling Ni,²² Thomas G. Brink,¹⁰ Tinggui Wang,^{1,2} Weikang Zheng,¹⁰ Xinwen Shu,²³ Xuechen Zheng,²⁴ Xiaozhi Lin,^{1,2} Xu Kong,^{1,2} Yijun Wang,^{17,18} Yibin Luo,^{1,2} and Zheyu Lin^{1,2}

Received: July 14, 2025; Accepted: October 27, 2025; https://doi.org/10.1016/j.xinn.2025.101169

The Innovation 2026, Volume 7, Issue 3

¹Department of Astronomy, University of Science and Technology of China, Hefei, 230026, Anhui, China

²School of Astronomy and Space Science, University of Science and Technology of China, Hefei, 230026, Anhui, China

³National Astronomical Observatories, Chinese Academy of Sciences, Beijing, 100012, China

⁴Department of Astronomy, School of Physics, Peking University, Beijing, 100871, China

⁵Kavli Institute for Astronomy and Astrophysics, Peking University, Beijing, 100871, China

⁶Department of Physics, University of Hong Kong, Pokfulam Road, Hong Kong, China

⁷School of Physics and Astronomy, Sun Yat-sen University, Zhuhai, 519082, China

⁸CSST Science Center for the Guangdong-Hong Kong-Macau Greater Bay Area, Sun Yat-sen University, Zhuhai, 519082, China

⁹Department of Physics, Tsinghua University, Beijing, 100084, China

¹⁰Department of Astronomy, University of California, Berkeley, CA 94720-3411, USA

¹¹Instituto de Astrofísica, Facultad de Física and Centro de Astroingeniería, Pontificia Universidad Católica de Chile, Santiago, 7820436, RM, Chile

¹²Millennium Institute of Astrophysics, Santiago, 7500011, RM, Chile

¹³Space Science Institute, Boulder, 80301, CO, USA

¹⁴Dipartimento di Fisica e Astronomia "Augusto Righi", Università degli Studi di Bologna, Via Gobetti 93/2, Bologna, 40129, Italy

¹⁵INAF – Osservatorio di Astrofisica e Scienza dello Spazio di Bologna, Via Gobetti 93/3, Bologna, 40129, Italy

¹⁶Department of Astronomy, University of Michigan, 1085 S University, Ann Arbor, MI 48109, USA

¹⁷School of Astronomy and Space Science, Nanjing University, Nanjing, 210093, China

¹⁸Key Laboratory of Modern Astronomy and Astrophysics (Nanjing University), Ministry of Education, Nanjing, 210093, China

¹⁹Department of Astrophysics/IMAPP, Radboud University Nijmegen, P.O. Box 9010, Nijmegen, 6500 GL, The Netherlands

²⁰Department of Astronomy, Xiamen University, Xiamen, 361005, Fujian, China

²¹Department of Astronomy, School of Physics, Huazhong University of Science and Technology, Wuhan, 1037, Hubei, China

²²Max-Planck-Institut für extraterrestrische Physik (MPE), Gießenbachstraße 1, Garching bei München, D-85748, Germany

²³Department of Physics, Anhui Normal University, Wuhu, Anhui 241002, China

²⁴Shanghai Astronomical Observatory, Chinese Academy of Sciences, Shanghai, 200030, China

^{*}Correspondence: xuey@ustc.edu.cn

^{**}Correspondence: lishuo@nao.cas.cn

GRAPHICAL ABSTRACT



PUBLIC SUMMARY

- The source has the best X-ray coverage spanning ~ 20 years with the deepest total exposure of ~ 10 Ms.
- The source is the faintest X-ray-selected tidal disruption event (TDE) to date.
- The source displays unusually strong hard X-ray emission and extreme luminosity variability.
- The source is likely the most distant supermassive black hole binary TDE known to date.

ABSTRACT

Tidal disruption events (TDEs), which occur when stars enter the tidal radii of supermassive black holes (SMBHs) and are subsequently torn apart by their tidal forces, represent intriguing phenomena that stimulate growing research interest and pose an increasing number of puzzles in the era of time-domain astronomy. Here we report an unusual X-ray transient, XID 935,

discovered in the 7 Ms Chandra Deep Field-South, the deepest X-ray survey ever. XID 935 experienced an overall X-ray dimming by a factor of more than 40 between 1999 and 2016. Not monotonically decreasing during this period, its X-ray luminosity increased by a factor > 27 within 2 months, from $L_{0.5-7~\rm keV} < 10^{40.87}$ erg s $^{-1}$ (10 October 2014 - 4 January 2015) to $L_{0.5-7~\rm keV} = 10^{42.31\pm0.20}$ erg s $^{-1}$ (16 March 2015). The X-ray position of XID 935 is located at the center of its host galaxy with a spectroscopic redshift of 0.251, whose optical spectra do not display emission characteristics associated with an active galactic nucleus. The peak 0.5–2.0 keV flux is the faintest among all the X-ray-selected TDE candidates to date. Thanks to a total exposure of ~ 9.5 Ms in the X-ray bands, we manage to secure relatively well-sampled, 20-year-long X-ray light curves of this deepest X-ray-selected TDE candidate. We find that a partial TDE model could not explain the main declining trend. An SMBH binary TDE model is in acceptable accordance with the light curves of XID 935; however, it fails to match short-timescale fluctuations exactly. Therefore, the exceptional observational features of XID 935 provide a key benchmark for refining quantitative TDE models and simulations.

KEYWORDS

Tidal Disruption Event, Supermassive Black Hole Binary, X-ray Transient

INTRODUCTION

In the early 1960s, the first quasi-stellar object (i.e., quasar) was discovered. [1] One possible power source of quasars was suggested [2] to be the tidal disruption of a star passing within the Roche limit of a supermassive black hole (SMBH), now known as a tidal disruption event (TDE). Later detailed research demonstrated that TDEs cannot release sufficient sustained energy to explain the persistent activity of an active galactic nucleus (AGN). [3,4] Nonetheless, an order of 10^6 stars are sacrificed over the lifetime of a galaxy, [5] so disrupted stars may not contribute significantly to the growth of an SMBH with a mass larger than $10^7~M_{\odot}$, TDEs may affect the spin distribution for BHs with mass $\sim 10^6~M_{\odot}$ [6] and power observed AGNs in dwarf galaxies. [7] Although TDEs lost to galactic-scale gas [8,9,5] in the race for providing fuel to AGNs, their unique

characteristics are still an outstanding probe for revealing dormant SMBHs.^[10] Since NGC 5905 was first noticed, ^[11] over one hundred TDEs have been discovered, and probed with respectable amounts of multi-wavelength data. Recently, time-domain surveys^[12,13] have propelled TDE research into a new era of proactive exploration, rather than relying on serendipitous discoveries in legacy data.

The TDE model described in Rees (1988)^[10] neglects partial stellar disruptions, now known as the partial TDE (pTDE), in which the pericenter of the star is slightly farther from the tidal radius, resulting in a surviving stellar core after the encounter.^[14] In the case of pTDE, the power law of the fallback rate is predicted to be steeper, $\propto t^{-9/4}$,^[15] compared to complete disruption, $\propto t^{-5/3}$.^[16] Furthermore, a remnant core has the potential to produce a second TDE if it becomes bound to the SMBH after the first encounter.^[17]

A regular TDE usually refers to the stellar disruption by a single quiescent SMBH lying at the center of a galaxy. [10,16,18] However, special TDEs occurring in SMBH binaries (SMBHBs) have been proposed, [19] which exhibit interrupted tidal flares caused by the companion black hole, compared to the power-law decay light curve (i.e., $\propto t^{-5/3}$). [16] SDSS J120136.02+300305.5 (hereafter SDSS J1201+30), [20] whose deep dips in its ~ 300 -day evolving X-ray light curve could be explained by the SMBHB TDE model, is the first SMBHB TDE candidate with a spectroscopic redshift of $z_{\rm spec}=0.146$. Recently, a second X-ray candidate at $z_{\rm spec}=0.1655$ with a ~ 550 -day X-ray light curve, OGLE16aaa, was reported. [21] Both SDSS J1201+30 and OGLE16aaa exhibit apparent interruptions in their soft X-ray light curves, which can be explained by the companion black hole perturbing the fallback rate of disrupted debris. The 0.2–2.0 keV X-ray flux of SDSS J1201+30 decreased by more than 47 times within 7 days, while the 0.3–2.0 keV X-ray emission was observed in either source.

To date, most X-ray TDEs have been discovered through the detection of soft X-ray flares, produced by emission from the transient accretion disk formed after the circularization of stellar debris. Near peak luminosities, the X-ray spectra of these TDEs are well fitted by either a black-body with a temperature of $kT_{\rm bb}=0.04-0.12$ keV or a power law with an index of $\Gamma_X=4-5$, followed by a spectral hardening over time.^[22] In addition, there is another rare population of X-ray TDEs characterized by much harder spectra, extremely high X-ray luminosities, and dramatic

short-time variability. [18,23] They are believed to be produced by powerful relativistic jets aligned with our line of sight, rather than by accretion.

Here, we report an unusual X-ray transient, XID 935 (${\rm RA_{J2000}}=53.248664^\circ$, ${\rm Dec_{J2000}}=-27.841828^\circ$, with a 1- σ positional accuracy of 0.3 arcsec), discovered in the deepest X-ray survey ever—the 7 Ms Chandra Deep Field-South (CDF-S), [24,25] whose extraordinary observational properties make it the deepest X-ray-selected TDE candidate. We use a cosmology of $H_0=70~{\rm km~s^{-1}~Mpc^{-1}}$, $\Omega_M=0.27$, and $\Omega_\Lambda=0.73$.

MATERIALS AND METHODS

X-ray data

Data reduction

The CDF-S^[24] and Extended-CDF-S (E-CDF-S; 250-ks depth)^[26,27] surveys include a total of 111 Chandra observations performed between 1999 and 2016. The XMM deep survey in the CDF-S (XMM-CDFS; 3-Ms depth)^[28] consists of 33 observations carried out between 2001–2002 and 2008–2010. The Wide-CDF-S (W-CDF-S; 29-ks depth)^[29] has one observation covering the position of XID 935. Table S1 lists the observation identification number (ObsID), date, exposure, and bin name of these X-ray observations. Observation 581 is not included in the CDF-S due to telemetry saturation, but XID 935 is located on CCD I0 which escaped this disaster. All CDF-S and XMM-CDFS observations cover the position of XID 935. The E-CDF-S consists of four distinct sub-fields with only the edges overlapping between them, so only 3 (ObsIDs = 5021, 5022, and 6164) out of its 9 observations observed XID 935 and are included in this work. ROSAT^[30] and Swift^[31] observations are listed in Table S2.

CIAO 4.14 with CALDB 4.9.7 was utilized to process the cleaned event files from the 7 Ms CDF-S^[24] and E-CDF-S.^[27] The *dmellipse* of CIAO was used to generate an elliptical source region that encloses 90% of the flux. The background region is an annulus with an inner radius of $R_{\rm in}=12''$ and an outer radius of $R_{\rm out}=40''$. According to the 7 Ms CDF-S catalog, six sources were masked since they are immediately adjacent to the background region of XID 935, as shown in Figure S2. In certain observations, the background region overlapped with the

CCD gap, and these areas were masked using box regions. Spectral files were generated by the CIAO tool *specextract* and combined using *combine_spectra* according to the time bins specified in Table S1. The parameter *correctpsf* in *specextract* was set to yes for aperture correction.

SAS 21.0.0 was utilized to obtain cleaned event files of XMM-CDFS observations following the threads of sas-thread-startup, sas-thread-epic-reprocessing, and sas-thread-epic-filterbackground. Subsequently, the spectra were extracted using the spectral analysis threads of MOS (sas-thread-mos-spectrum) and PN (sas-thread-pn-spectrum). The source region is a circle with a radius of 10'' (corresponding to 60% encircled energy at 1.5 keV), and the background region is an annulus with an inner radius of $R_{\rm in}=25''$ and an outer radius of $R_{\rm out}=60''$. According to the 7 Ms CDF-S catalog, nine sources were masked with a circle with a radius of 20'', since they overlap with the background region of XID 935, as shown in Figure S3. The arfgen applied default aperture corrections for point sources. The spectral combination was performed by the SAS tool epicspeccombine according to the time bins listed in Table S1.

Xselect of HEASoft was used to extract the spectra from the event files of ROSAT and Swift (see Table S2 for ObsIDs). XID 935 is not detected in the ROSAT All-Sky Survey (RASS) observations conducted between June 1990 and August 1991. For Swift, the source region is a circle with a radius of R=30'' and the background region is an annulus with an inner radius of $R_{\rm in}=40''$ and an outer radius of $R_{\rm out}=80''$. For ROSAT, the region configuration is the same as that of Swift, but R=60'', $R_{\rm in}=70''$ and $R_{\rm out}=120''$. The arf file was generated using *xrtmkarf* of HEASoft for Swift, with a setting parameter *psfflag* = *yes* to correct the point spread function for point-like sources. The *pcarf* of HEASoft was used to generate the arf file for ROSAT, with an aperture-correction factor of 0.94 based on the encircled energy function. For eROSITA, [32] the eROSITA-DE Data Release 1 archive supports a tool for the upper limit for a single position.

Bin strategies

The significance of source detection is calculated using the likelihood-ratio test (LRT), [33] see Listing S1. For p-values larger than 0.0027, the flux/luminosity is considered as the upper limit at the 90% confidence level. For p-values below this threshold (i.e., $\geq 3 \sigma$), the flux/luminosity is reported as the mean value with a 1- σ uncertainty. Two different binning strategies for the light curve are applied to the Chandra and XMM-Newton data:

A. 1-month binning:

(1) For both Chandra and XMM-Newton observations, a 1-month-bin scheme is initially applied for a straightforward overall view of the light curves (see Figure S4 for a flow diagram and Figure S5 for the 1-month-bin light curves).

B. adaptive binning:

- (1) Observations are marked as detected points if the significance of likelihood-ratio test in the full band is greater than 3 σ , and as non-detected points if the significance is less than 3 σ .
- (2) For non-detected points, a 1-month-bin scheme is applied, but it stops at any detected point (see Figure S6 for a flow diagram). New bins are marked as non-detected points if the significances of likelihood-ratio tests in the full, soft, and hard band are all less than 3 σ ; otherwise, they are marked as detected points.
- (3) For detected points (both from step 1 and step 2), a 1-month-bin scheme is applied, but it stops at any non-detected point. If the right margin of a bin coincides with the exposure duration of a point, the right margin is set as the start time of that point.
- (4) Some data remain non-detection even after one-month binning. For these non-detected points, a 4-months-bin scheme is applied, but it stops at any detected point. New bins are marked as non-detected points if the significances of likelihood-ratio tests in the full, soft, and hard band are all less than 3 σ ; otherwise, they are marked as detected points.

Spectral fitting

Given that XID 935 has low counts in most observations, it is not suitable to fit those spectra. The *aprates* of CIAO is used to calculate the count rate, then *modelflux* of CIAO is used to calculate the flux using this count rate, and subsequently the luminosity is derived from this flux. For modelflux, the parameters model = "xspowerlaw.pow1", absmodel = "xsphabs.abs1", absparams = "abs1.nH = 0.008" [34] and paramvals = "pow1.PhoIndex = 2.4" are based on the spectral fitting result through stacking all XID 935 Chandra observations. The cosmology model is set as the default one in XSPEC. Figure 1 shows the adaptive-bin scheme light curves; data listed in Table S4. Spectral fitting is only performed for the spectrum with net counts larger than 60 (see Table S3, and Figure S7). To fit the spectrum for a weak source, especially with low counts in its background, a better grouping strategy is to ensure that each bin in the background

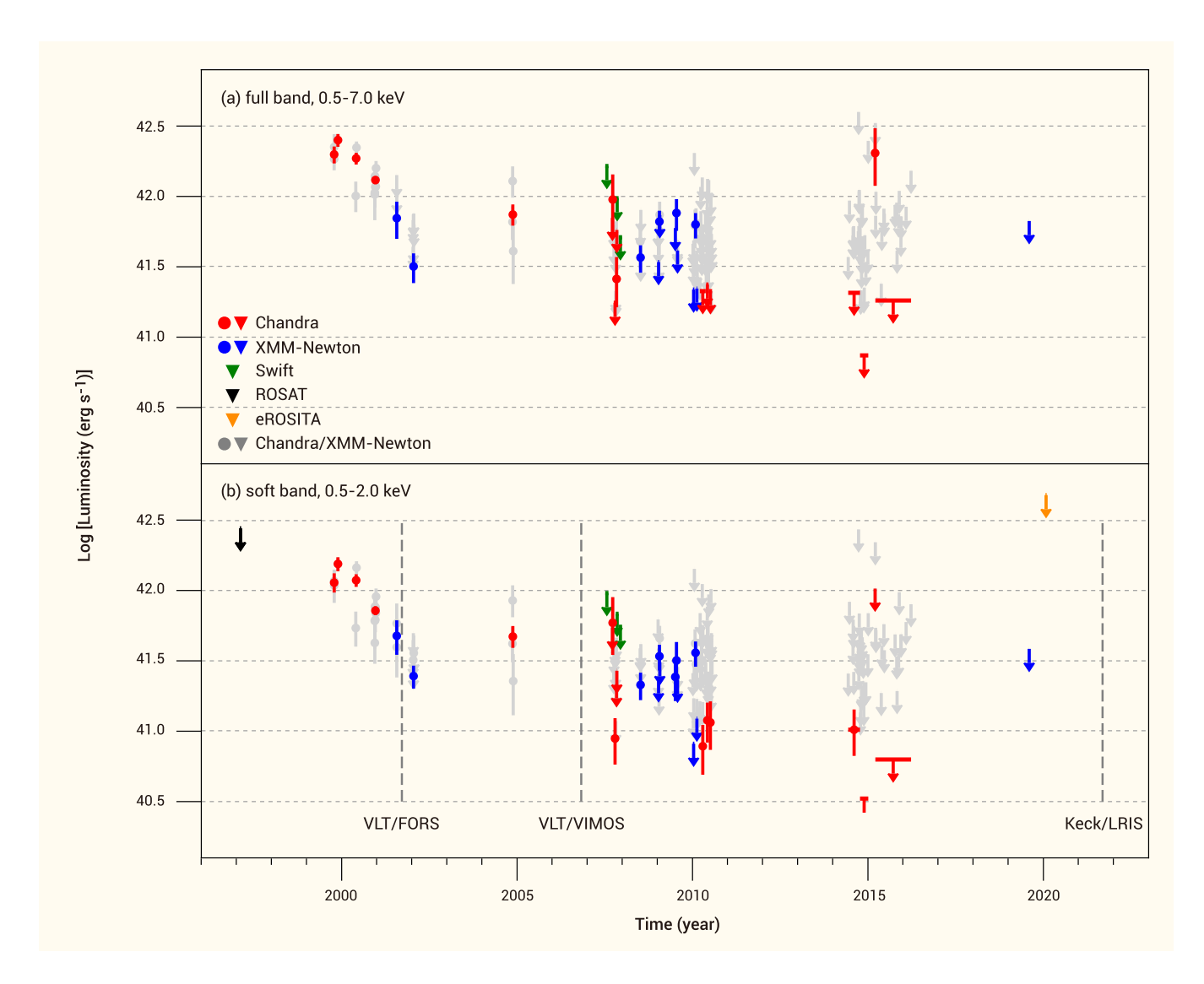


Figure 1: Adaptive-bin X-ray light curves of XID 935. (a) Light curve in the rest-frame 0.5-7.0 keV band (full band, containing 768.9 ± 43.3 and 905.0 ± 84.0 Chandra and XMM-Newton net counts, respectively). (b) Light curve in the rest-frame 0.5-2.0 keV band (soft band, containing 595.9 ± 28.5 and 680.7 ± 62.6 Chandra and XMM-Newton net counts, respectively). Red, dark blue, green, black, and orange data are from Chandra, XMM-Newton, Swift, ROSAT, and eROSITA, respectively. Grey data represent individual observations of Chandra and XMM-Newton. Horizontal bars indicate ranges of time bins. Arrows indicate 90%-confidence-level upper limits. The data gaps between 2002–2004 and 2005–2007 indicate no X-ray observational coverage. Dashed lines denote the observation times of optical spectra.

spectrum contains at least one count to use the W statistic.^[35] The HEASoft tool *ftgrouppha* supports this grouping by setting the parameter grouptype = bmin and groupscale = 1. The XSPEC 12.13.0 software was used to fit the regrouped spectra derived from both Chandra and XMM-Newton observations. We apply a Galactic and intrinsic absorbed redshifted power-law model, $tbabs \times ztbabs \times zpowerlw$, to the spectra of XID 935, with the Galactic column density fixed at $N_{\rm H} = 8.8 \times 10^{19}~{\rm cm}^{-2}$, redshifts of zpowerlw and ztbabs fixed at z = 0.251, power-law photon index and redshifted $N_{\rm H}$ left free to vary. The best-fit column density during these bins was always $N_{\rm H} < 10^{22}~{\rm cm}^{-2}$ (see Section Exclusion of a variable absorption origin), which implies that the absorption is not severe in these periods.

UV/optical data

The UV/optical observations of XMM/OM and Swift/UVOT were performed for XID 935. The HEASoft tool *uvotimsum* was utilized to sum the Swift/UVOT UV/optical observations and the SAS tool *ommosaic* was used to sum the XMM/OM UV/optical observations. Photutils^[36] was used to perform aperture photometry (a circle with a 4" radius for the source region; an annulus with a 6" inner radius and a 10" outer radius for the background region) on the summed UV/optical images. The aperture correction factors are 0.65, 0.7, 0.7, and 0.8 for XMM/OM UVW2, UVM2, UVW1, and u bands, respectively. For Swift/UVOT UVW2, UVM2, UVW1, and u bands, the aperture correction factor is all 0.95. The results are shown in Figure S1.

Host SED fitting

The SED fitting was performed using CIGALE^[37] with the following multi-wavelength data: WFI_B , WFI_V , WFI_R , WFI_I , WFI_J , WFI_J , WFI_H , WFI_K , spitzer.irac.ch1 (3.6 μm), spitzer.irac.ch2 (4.5 μm), spitzer.irac.ch3 (5.8 μm), spitzer.irac.ch4 (8.0 μm); [38] spitzer.mips.24 (24 μm); [39] spitzer.mips.70 (70 μm); [40] scuba.850 (850 μm); [41] and $Swift_UVOT.UVW2$, $Swift_UVOT.U$ $Swift_UVOT.UVW1$, $Swift_UVOT.U$ bands obtained as described in Section UV/optical data. For each band, based on A_f/A_v ((SVO Filter Profile Service:http://svo2.cab.inta-csic.es/theory/fps/) and $A_v = R_v * E(B-V)$, setting E(B-V) = 0.0072, assuming $R_v = 3.1$, the A_v has been calculated and applied in Galactic extinction correction. Table S6 lists the CIGALE parameters used

in our fitting and Figure 2 shows the fitting result. We use GALFIT^[42] to decompose the bulge

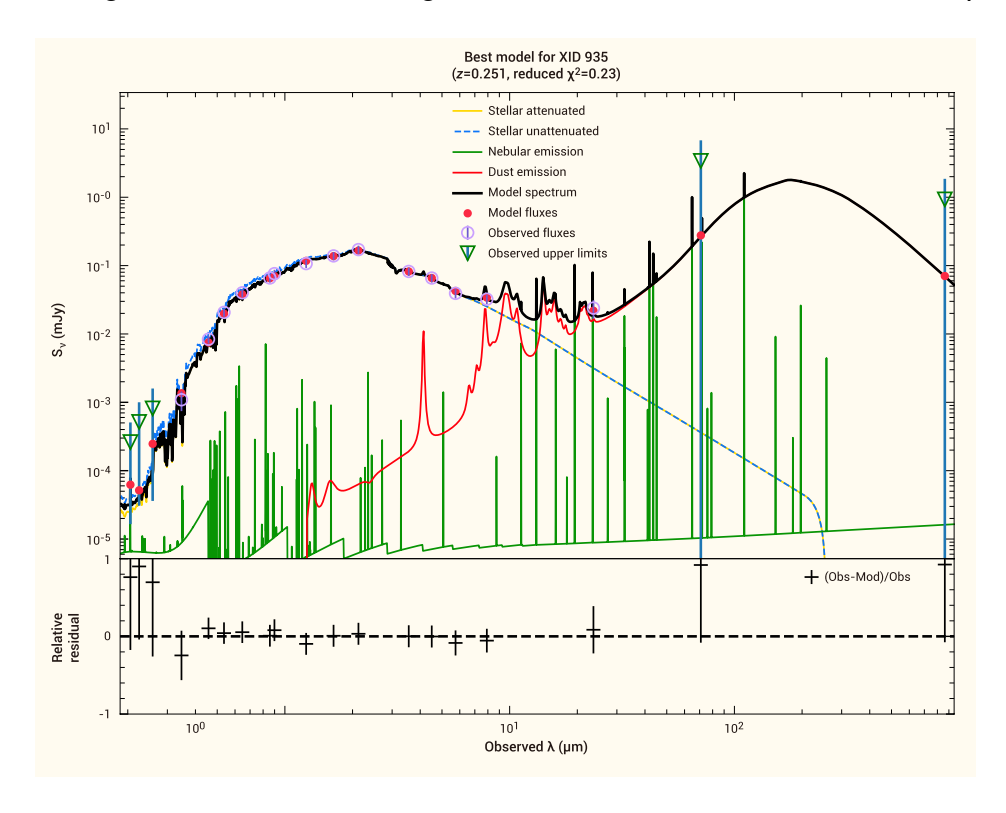


Figure 2: **SED** fitting result for XID 935 using CIGALE. The stellar mass $M_{\star} = (3.1 \pm 0.6) \times 10^{10}~M_{\odot}$ and the star-formation rate SFR< $1.3 \times 10^{-2} M_{\odot}$ /year (90% confidence level) were obtained. Note that an AGN component is not required in the fitting.

and disk components of images in the WFI_B , WFI_V , WFI_I , and WFI_z bands. SED fitting for the bulge reveals no significant difference from the total galaxy.

Optical spectral reduction

To pin down the nature of XID 935 whose temporal evolution could be due to the AGN variability, we obtained an optical spectrum of the source with the Keck I telescope at the W. M. Keck Observatory and the Low Resolution Imaging Spectrometer (LRIS; 43) on UT2021-09-08 14:30 (MJD 59465.6045). A total of 850 s and 450 s \times 2 exposures were obtained through the LRIS blue- and the red-arm CCDs, respectively. The combination of the 5600 Å dichroic, the 600/4000 blue grism (with a 0.63 Å pixel $^{-1}$ dispersion) and the 400/8500 red grism (with a 1.20 Å pixel $^{-1}$ dispersion), together with a 1" slit width provided an observed wavelength coverage of 3150–10270 Å. The spectral resolution near the central wavelength of the blue and the red arms yields, $R_{\rm blue} \sim$ 942 and $R_{\rm red} \sim$ 844, corresponding to \sim 4.7 Å and \sim 9.4 Å resolution element in the blue and the red arms, respectively. During the observation, the slit was aligned to the parallactic

angle, which is ≈ -5 degrees from the North. The raw LRIS spectral data were processed by the fully automated LPipe pipeline. The spectra were dominated by absorption lines without prominent emission lines, indicating the absence of significant AGN activity. To assess the upper limits of AGN activity, we calculated the upper limits of [OIII] as follows. The Keck/LRIS spectrum was first corrected for Galactic extinction using the dust map of Schlafly et al. (2011) and the extinction curve from Fitzpatrick et al. (1999). The starlight continuum was then modeled using the Python package pPXF of Cappellari et al. (2004) and Cappellari et al. (2017), which enables the extraction of stellar population and kinematics through penalized fitting. Figure 3 shows the optical spectra. After subtracting the modeled continuum from the spectrum, we

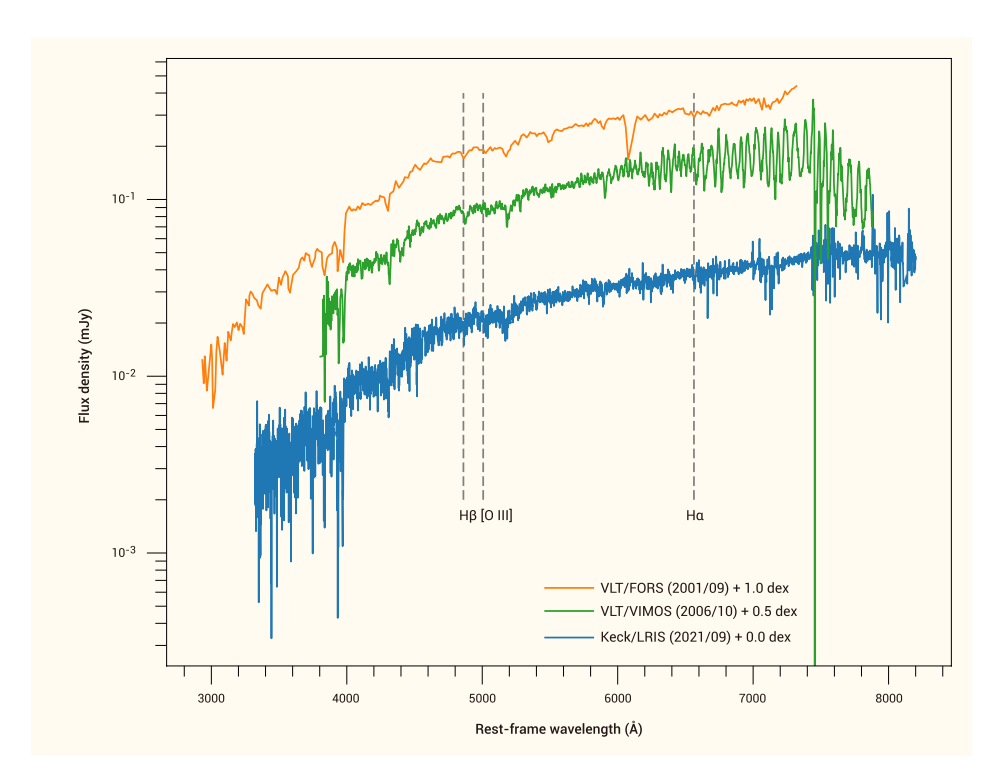


Figure 3: **Optical spectra of XID 935.** The spectral analysis of the Keck/LRIS spectrum (blue), performed on 8 September 2021, shows that the host galaxy of XID 935 has no significant AGN characteristics. The flux upper limit of the [O III] emission line is $10^{-16.68}$ erg s⁻¹ cm⁻² and the stellar velocity dispersion is 138 ± 31 km/s. The VLT/VIMOS spectrum (green) was obtained on 30 October 2006 (Balestra et al. 2010). The VLT/FORS spectrum (orange) was observed on 18-20 September 2001 (Szokoly et al. 2004).

calculated the [OIII] upper limits at a 90% confidence level using the method outlined in Avni et al. (1976), [49] assuming a pseudo-width of [OIII] from composite spectra of Vanden et al. (2001). [50]

Numerical modeling

To verify whether the SMBHB TDE model can explain the observed results, we conducted a series of numerical simulations for comparison with the observational data. The numerical model is based on three-body scattering experiments. Here, we briefly introduce our modeling approach. For more details, please refer to Liu et al. (2009) and Liu et al. (2014).^[19,20]

We assume that a star on a parabolic orbit is tidally disrupted at the pericenter $r_{\rm p}$. The specific energy E of the stellar debris after disruption ranges from $-E_{\rm b}-\Delta E$ to $-E_{\rm b}+\Delta E$, where $E_{\rm b}$ is the orbital binding energy of the star, ΔE is the spread in specific energy. [10,51] For a star on the parabolic orbit, nearly half of the debris is bound to the SMBH after the tidal disruption. As a result, the specific energy of the bound debris ranges from $-\Delta E$ to 0. We assume that the disrupted star is constructed as polytropes with a solar mass. And the mass distribution of the debris can be assumed to be constant. [51] To simplify the calculation, we neglect the interactions between debris elements. As a consequence, each element follows a ballistic trajectory. Thus we can perform scattering experiments for each three-body system composed of the binary black holes and the debris element. Although this simplification is less precise than full hydrodynamical simulations, it provides a sufficiently accurate approximation for order-of-magnitude estimates and qualitative analysis.

From the scattering experiment results, it is easy to estimate the rate at which the debris returns to the vicinity of the black hole, namely the mass fallback rate. Assuming that the fallback rate is proportional to the X-ray emission, we can make the conversion factor η as a free parameter and fit it to the observed flux. By comparing the "light curve" derived from the scattering experiments (more precisely, the fallback curve) with the observational data, we can infer the approximate time of disruption based on the position of the peak along the time axis. This gives us $T_{\rm delay}$, the delay between the actual disruption and the first effective observational detection.

It should be noted that the methodology described above may lead to multiple sets of parameters that fit the data. Our analysis serves to qualitatively evaluate the plausibility of the SMBHB TDE model in explaining the observations, rather than to exactly determine the system's actual orbital parameters.

RESULTS AND DISCUSSIONS

Light curves and spectra

XID 935 was originally detected in the first 1 Ms observations of the CDF-S, [52] with an optical counterpart subsequently classified as an inactive galaxy showing only absorption lines with $z_{
m spec}=0.251$ based on a VLT/FORS optical spectrum obtained on 18–20 September 2001^[53] as shown in Figure 3. Luo et al. (2017)[24] classified XID 935 as an AGN based on the entire 7 Ms CDF-S data. Zheng et al. (2017)[54] found six candidate transients based on the criterion that the flux change exceeds $3-\sigma$ of the average flux, using the 3-month-bin 7 Ms CDF-S light curves. Three of these candidates (XID 725, [55] XID 330, [56] and XID 403 [57]) have been reported in the literature. XID 935 is among these six candidate transients and is reclassified as a long outburst transient. XID 935 was additionally observed as part of the E-CDF-S (250-ks depth), [26,27] the XMM-CDFS (3-Ms depth), [28] the W-CDF-S (29-ks depth), [29] Swift (0.5-Ms depth), [31] ROSAT (8.52-ks depth), [30] and eROSITA (0.218-ks depth), [32] providing relatively well-sampled 20-yearlong X-ray light curves of XID 935. Unlike the 3-month bin scheme adopted by Zheng et al. (2017), [54] we use an adaptive-bin scheme to obtain light curves (see Figure 1; data listed in Table S4), given that some interrupted flares that are shorter than 3-month time scale will be smoothed out and that stacking adjacent non-detection observations could increase the detection sensitivity.

Below we summarize the observational features of XID 935:

- (1) A peak soft X-ray luminosity of $L_{0.5-2~{\rm keV}}=10^{42.14\pm0.04}~{\rm erg~s^{-1}}$ was recorded in October-November 1999, dimming by a factor of at least 40 between November 1999 and October 2014;
- (2) Significant hard X-ray emission of $L_{2-7~{\rm keV}}=10^{42.09\pm0.12}~{\rm erg~s^{-1}}$ was detected in November 1999; however, there was almost no detection (< 3σ) of hard X-ray emission after December 2000 except on March 16, 2015;
- (3) It displays extreme and fast luminosity variations: the full-band (0.5–7.0 keV) X-ray luminosity increased by a factor of at least 27 within ~ 2 months, from a 90%-confidence-level upper limit of $L_{0.5-7~\rm keV} < 10^{40.87}$ erg s⁻¹ (10 October 2014 4 January 2015) to $L_{0.5-7~\rm keV} = 10^{42.31\pm0.20}$ erg s⁻¹ (16 March 2015);
 - (4) The X-ray emission is centered in the host galaxy, with no AGN characteristics (see Figure

- 3) or UV/optical variability (see Figure S1);
- (5) No radio emission was detected at 15 mm, ^[58] 6 cm, ^[59] 13 cm, ^[60] 21 cm, ^[61,62,63,64,65] 92 cm, ^[66] 1.25–3.75 m, ^[67] 1.5–3 m, ^[68] and 4 m bands, ^[69] as well as the Very Large Array (VLA) Survey of the CDF-S, ^[70] the VLA Survey of the GOODS-S, ^[71] the ultradeep radio imaging of GOODS-S/HUDF, ^[72] and the VLA Sky Survey (VLASS), ^[73] with no jet being detected.

Exclusion of a variable absorption origin

The X-ray variability could be attributed to intrinsic spectral variation and/or variable absorption. For an absorbed power-law model, with a power-law photon index of $\Gamma=2.4$ (derived from spectral stacking of Chandra observations listed in Table S1) and a column density of $N_{\rm H}=1\times10^{22}~{\rm cm^{-2}}$, a minimum of 60 full-band net counts are required for a reliable fit. However, since most of the bins for XID 935 have low counts, only seven bins contain full-band net counts exceeding 60, which are used to estimate the intrinsic absorption. A Galactic and intrinsic absorbed redshifted power-law model, $tbabs \times ztbabs \times zpowerlw$, is applied to these seven spectra, with the Galactic column density fixed at $N_{\rm H}=8.8\times10^{19}~{\rm cm^{-2}}$ [34] and the redshift fixed at z=0.251. [53] The power-law photon index and the redshifted $N_{
m H}$ are allowed to vary freely. The best-fit column density in these seven bins (see Table S3) was always less than 10^{22} cm⁻². If the X-ray variability were primarily driven by varying obscuration, a harder spectrum would be expected, as soft photons would be absorbed. However, after 2001, most bins of XID 935 show no detection in the hard band but significant detection in the soft band, suggesting a preference for soft spectra. When both the soft and hard bands show non-detection, it becomes challenging to disentangle the contribution from intrinsic spectral variation and variable absorption. Notably, the optical spectra of XID 935 show no characteristics of AGN activity, implying that there is little surrounding matter near the black hole. Hence, we assume that the X-ray variability of XID 935 is not caused by the variable absorption, and a Galactic-absorbed redshifted power-law model, $tbabs \times zpowerlw$, with fixed $N_{\rm H}=8.8 \times 10^{19}~{
m cm^{-2}}$, $\Gamma=2.4$, and z=0.251, is adopted to estimate the flux and luminosity (see materials and methods).

Exclusion of an AGN origin

It is not uncommon for AGNs to vary in brightness by several dozen times, either due to intrinsic spectral variation or variable absorption. Such sources typically exhibit persistent AGN signatures revealed by the strong narrow emission lines in their optical spectra. However, optical spectra of XID 935 obtained with VLT/FORS in September 2001^[53] and VLT/VIMOS in October $2006^{[74]}$ reveal no apparent AGN signature. We utilized Keck/LRIS to obtain a new optical spectrum of XID 935 on 8 September 2021 (see Figure 3 and materials and methods), which also shows no AGN signature. From the Keck spectrum, we estimate the 90%-confidence-level flux upper limit of the [O III] emission line, which is $f_{\rm [OIII]} < 10^{-16.68}$ erg s⁻¹ cm⁻². In addition, the ZTF r-band light curve shows no statistically significant variability over timescales of 5 years (see Figure S1). These findings suggest that the host galaxy of XID 935 is likely not an active galaxy. Some AGNs, known as "X-ray bright, optically normal galaxies" (XBONGs), ^[75] are X-ray bright but lack apparent AGN optical signatures. However, to our knowledge, no XBONG has shown X-ray variability by a factor of ≥ 40 . Moreover, the AGN scenario fails to account for the rapid luminosity changes discussed in point (3) of Section Light curves and spectra, so we exclude this possibility from further consideration.

Exclusion of an X-ray binary origin

X-ray binary (XRB) populations could also be a possible origin of hard X-ray emission. Using the stellar mass $[M_{\star}=(3.1\pm0.6)\times10^{10}~M_{\odot}]$ and the star formation rate (SFR< $1.3\times10^{-2}M_{\odot}$ yr $^{-1}$, at the 90% confidence level) derived from spectral energy distribution (SED) fitting (see materials and methods), and applying the relationship between XRB X-ray luminosity, stellar mass, SFR, and redshift, [76] we estimate the contribution of XRB populations to the X-ray emission of XID 935 to be $L_{2-10~{\rm keV}}({\rm XRB})=10^{40.22\pm0.30}~{\rm erg~s^{-1}}$. Apparently, this contribution is insufficient to account for the observed hard X-ray emission ($L_{2-7~{\rm keV}}\sim10^{42}~{\rm erg~s^{-1}}$). Moreover, due to the large number of XRBs, these populations as a whole are not expected to exhibit significant variability. Essentially no known individual extragalactic ultraluminous X-ray sources (ULXs) exhibit the required luminosity of $L_{2-7~{\rm keV}}\sim10^{42}~{\rm erg~s^{-1}}$, as ESO 243-49 HLX-1, [77] one of the most luminous ULXs known, attains only $L_{2-7~{\rm keV}}\sim10^{41}~{\rm erg~s^{-1}}$. Given that the number of galaxies in

the filed of view of 7 Ms CDF-S^[24] reaches 50539, the probability of a Galactic or local universe XRB aligning randomly with the core of a galaxy (within a 0.3'' radius) is about 0.79%. Therefore, XRB is not a reasonable explanation for XID 935.

TDE scenarios

Given the high level of its peak X-ray luminosity and its location at the center of its host galaxy, an edge-on disk galaxy (see Figure 4), it is reasonable to infer that the activity of XID 935 is linked to the central SMBH. As discussed above, the likelihood of XID 935 being an AGN is low. Consequently, a TDE emerges as a plausible scenario for XID 935. Observationally, XID 935 is

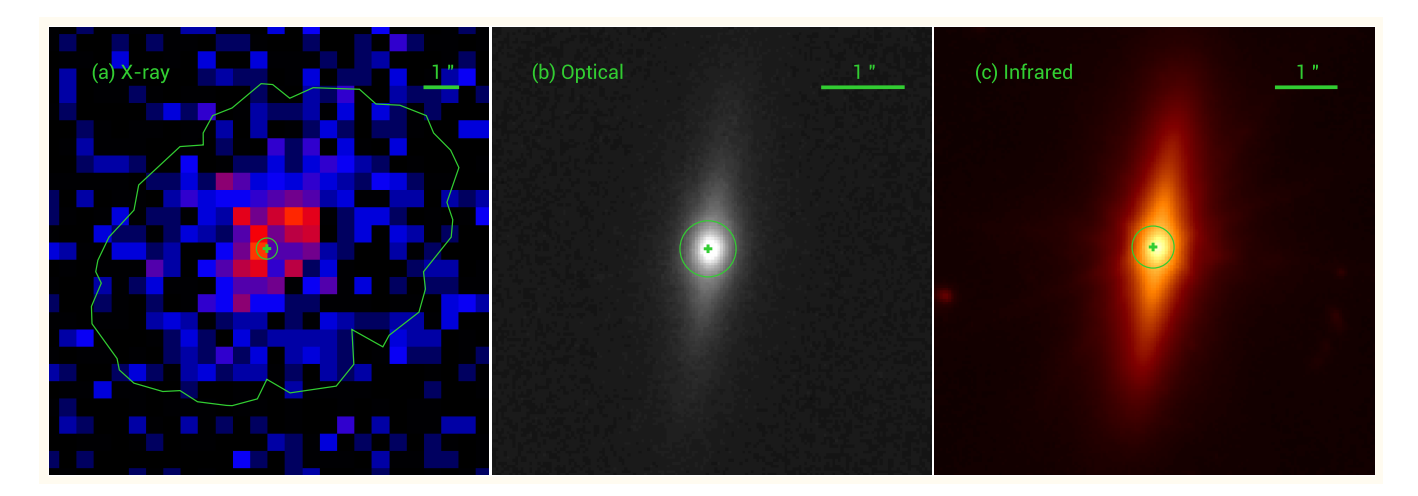


Figure 4: **Multi-wavelength images of XID 935.** (a) 7 Ms CDF-S image in the observed 0.5-7.0 keV band, with total net counts of 768.9 ± 43.3 . The green polygon is the 90% encircled-energy fraction region, centered at the source position (green plus; with a 1- σ positional accuracy of 0.3 arcsec, indicated by the green circle, corresponding to 0.99 kpc at z=0.251). (b) GOODS z band image. (c) JWST-NIRCam F227W band image. The green pluses and circles in Panels (b) and (c) are the same as that in Panel (a). The position of XID 935 is consistent with the nucleus of its host galaxy.

the observationally faintest X-ray-selected TDE candidate to date, as illustrated in Figure 5. The current X-ray observational capabilities remain inadequate for detecting enough faint TDEs like XID 935 at z>0.1 to enable systematic investigation of such TDEs at different redshifts. Thanks to the best X-ray coverage spanning over 20 years with the deepest total exposure of ~ 9.5 Ms, we can test the performance of TDE models on both long timescales and fine structural details.

Using the $M_{\rm BH}$ – σ_{\star} relation^[78] and stellar velocity dispersion $\sigma_{\star}=138\pm31~{\rm km~s^{-1}}$ measured from the Keck optical spectrum, we estimated an SMBH mass of $M_{\rm BH}=10^{7.45\pm0.88}~M_{\odot}$. A non-spinning SMBH with this mass can effectively tidally disrupt a main-sequence star (see Figure 1

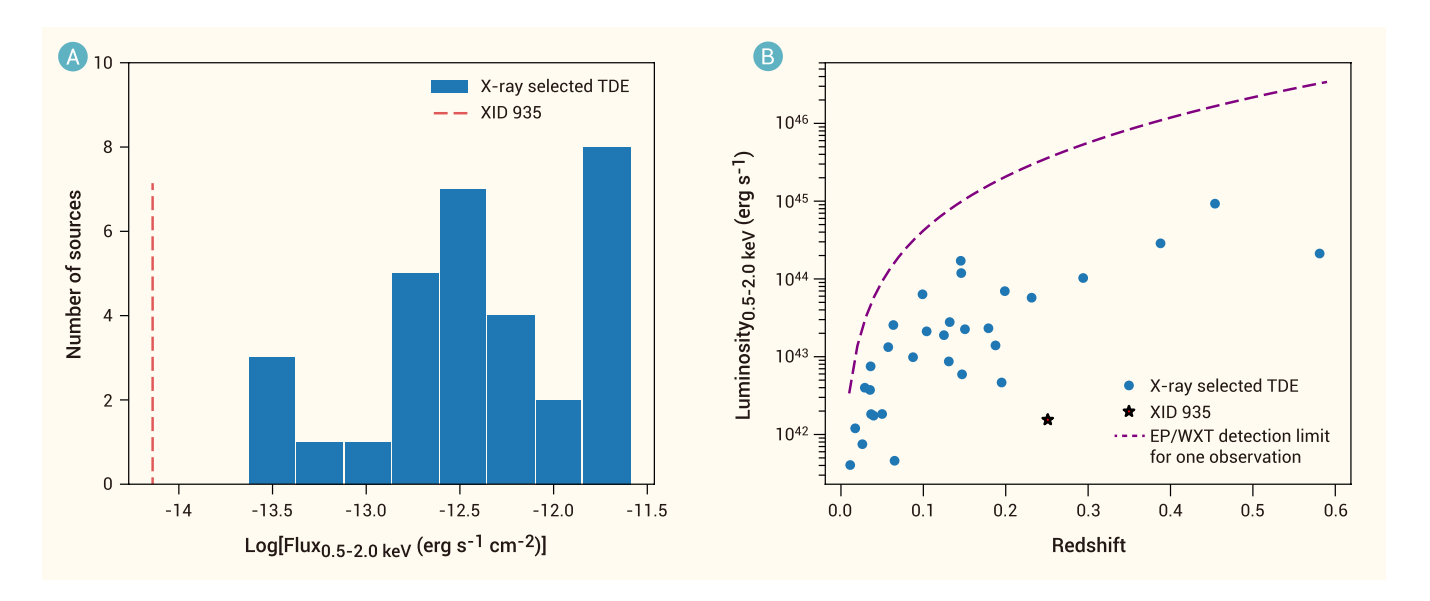


Figure 5: **X-ray-selected TDEs.** (a) Distribution of absorption-corrected peak 0.5–2.0 keV fluxes of X-ray-selected TDEs, with the vertical red dashed line highlighting XID 935. (b) Absorption-corrected peak 0.5–2.0 keV luminosities as a function of redshift, with XID 935 marked with a star symbol and other X-ray selected TDEs represented by blue points. The purple dashed curve is the 5-sigma detection limit of EP/WXT in an individual observation (i.e., 1.2-ks exposure).

in Gezari 2021). [79]

The full-band X-ray luminosity of XID 935 increased by a factor of at least 27 within ~ 2 months, from a 90% confidence level upper limit $L_{0.5-7~{\rm keV}} < 10^{40.87}~{\rm erg~s^{-1}}$ (10 October 2014 – 4 January 2015) to $L_{0.5-7~{\rm keV}} = 10^{42.31\pm0.20}~{\rm erg~s^{-1}}$ (16 March 2015). Table 1 shows the comparison between XID 935 and the two aforementioned SMBHB TDE candidates. Remarkably, the 16 March 2015

Table 1: Comparison between XID 935 and previous SMBHB TDE candidates

	XID 935	SDSS J1201+30	OGLE16aaa
Redshift	0.251	0.146	0.1655
Dimming degree	> 11 times (within 3 days)	>47 times (within 7 days)	
Flaring degree	> 27 times (within 70 days)		> 63 times (within 9 days)
Hard X-ray emission	Yes	No	No
Optical/UV variability	No	No	Yes

detection showed a significance of 3.16 sigma. It is challenging for both regular TDEs and AGNs to generate such notable luminosity changes within such short timeframes, [79,80] making the 16 March 2015 detection more appropriately treated as anomalous cases in both scenarios. However, SMBHB TDEs could bring about such alterations in the accretion state due to the companion black hole perturbing the fallback rate of disrupted debris. [20] Indeed, the SMBHB TDE model [19] can qualitatively describe the main trend of the XID 935 soft-band light curve, with three example sets of parameters being favored by the observations (see Figure 6 and Section

Numerical modeling for details). These results show different time delays $(T_{\rm delay})$ between the first observational detection point and the moment of TDE occurrence, different ellipticities of SMBHB orbit, the same primary SMBH of $M_{\rm BH}=2.0\times10^7~M_{\odot}$, different mass ratios between the secondary and primary SMBHs, different penetration factors, and the same orbital period of the SMBHB (see Liu et al. $2014^{[20]}$ for more details about parameters.) The relatively smooth decays observed in 2000–2002 and 2008–2010 could be reasonably explained by the regular TDE accretion stage in the SMBHB TDE model. The drop in 2015–2016 can be attributed to the perturbation of the TDE streams by the companion SMBH. However, this SMBHB TDE model is based on a simplified assumption that the bound debris of the TDE is regarded as free-moving particles, ignoring self-gravity and pressure. Hence, it cannot predict the fine structures of the light curve after several orbital periods, e.g., the fluctuations during January–July 2009 and drop during September–November 2007 (see Figure 6). A more physical SMBHB TDE model capable of explaining the fine structures of the light curve is desired. Additionally, the data gaps (i.e., no observational coverage) between 2002–2004 and 2005–2007 further complicate model validation.

The light curve of XID 935 during 1999–2002 shows a relatively smooth and steep ($\propto t^{-2.38}$) decline, suggesting a likely pTDE ($\propto t^{-9/4}$). In contrast to complete disruption, a stellar core survives in the pTDE scenario, leading to a fallback rate that is steeper than $t^{-5/3}$. The circularization process [81,82,83] seems to be a possible interpretation of the early behavior of XID 935 during 1999–2002. However, in the circularization process, even a black hole with a low mass of $M_{\rm BH}=10^6~M_{\odot}$ would not sustain a 1000-day decline. Given that XID 935 has $M_{\rm BH}\sim 10^{7.45\pm0.88}~M_{\odot}$, the circularization process is expected to be highly efficient, with a timescale described by

$$t_{\rm cir} = 7 \,\beta^{-4} \left(\frac{M_{\rm BH}}{10^{7.45} \, M_{\odot}} \right)^{-7/6} \left(\frac{M_*}{M_{\odot}} \right)^{-4/3} \left(\frac{R_*}{R_{\odot}} \right)^{7/2} \, \rm days. \tag{1}$$

 $t_{\rm cir}$ is given by the combination of equations (4) and (10) in Chen & Shen (2021). [83] Consequently, circularization is unlikely to be the primary mechanism driving the flare observed in XID 935. Nevertheless, the efficient circularization suggests that stream-stream collisions could rapidly lead to the formation of a compact accretion disk. As a result, the X-ray emission is

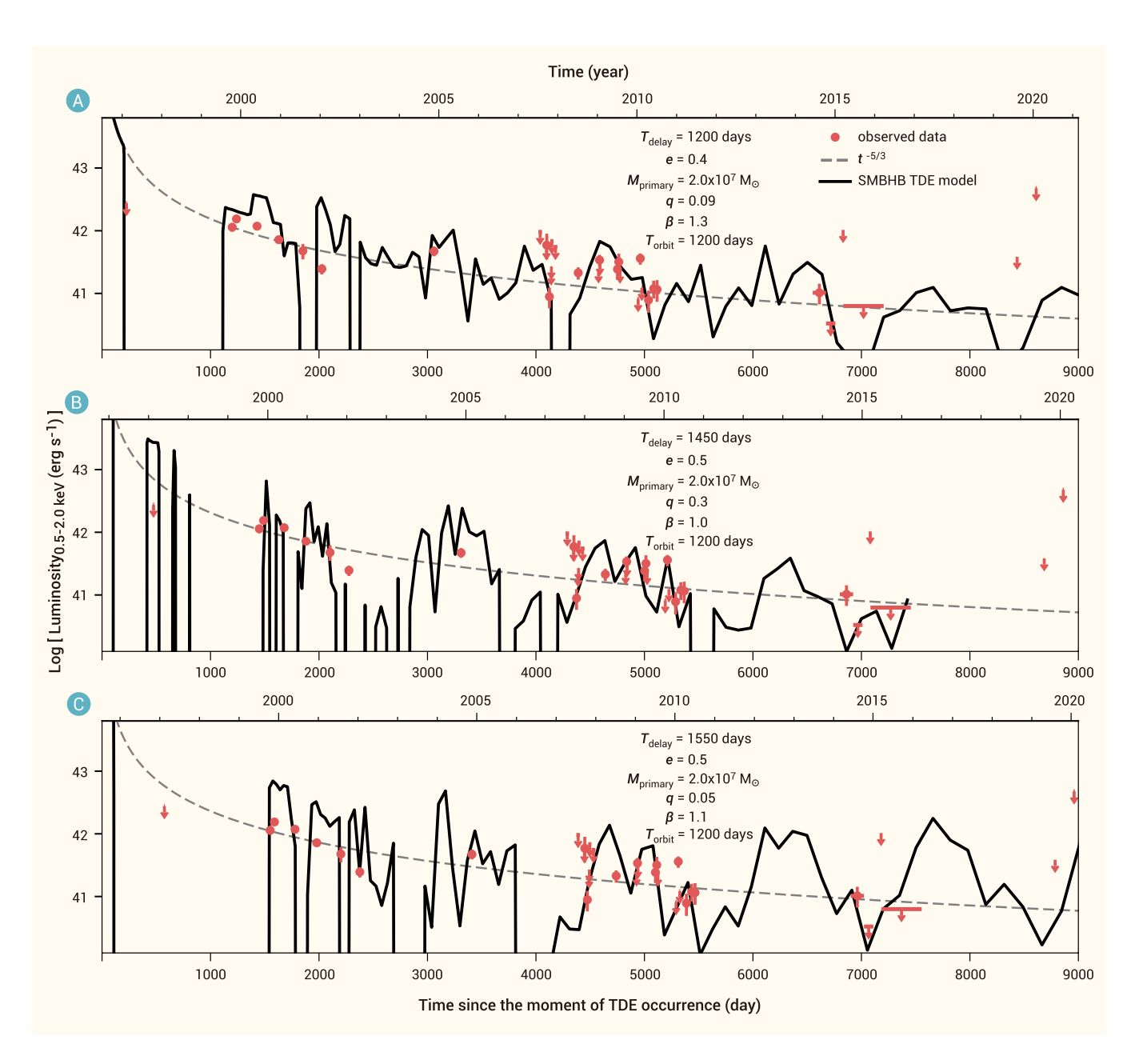


Figure 6: **SMBHB TDE model fits for XID 935.** In each panel, the rest-frame 0.5–2.0 keV light curve is shown with red symbols. Error bars correspond to 1- σ uncertainties. Downward arrows are 90%-confidence-level upper limits. The dashed grey curve represents the canonical $t^{-5/3}$ decay law. The gapped black solid curve is the SMBHB TDE model fitting result, with the following model parameters annotated: $T_{\rm delay}$, the time delay between the first observed detection data point and the moment of TDE occurrence; e, the ellipticity of SMBHB orbit; $M_{\rm primary}$, the mass of the primary black hole; q, the mass ratio between the secondary and primary SMBHs; β , the penetration factor; $T_{\rm orbit}$, the orbital period of SMBHB. (A) $T_{\rm delay}=1200$ days, e=0.4, q=0.09, $\beta=1.3$. (B) $T_{\rm delay}=1450$ days, e=0.5, q=0.3, $\beta=1.0$. (C) $T_{\rm delay}=1550$ days, e=0.5, q=0.05, $\beta=1.1$. (A),(B), and (C) share identical values of $M_{\rm primary}=2.0\times10^7~M_{\odot}$ and $T_{\rm orbit}=1200$ days.

predominantly governed by the disk accretion process. Furthermore, the hard X-ray spectrum observed during the early phase appears to originate from the accretion disk or its corona, rather than from the circularization process, which is typically associated with optical/UV emission rather than X-rays.^[84]

CONCLUSIONS

We report on a TDE candidate, XID 935, in the 7 Ms CDF-S. XID 935 has the faintest peak 0.5–2.0 keV X-ray flux among all X-ray-selected TDEs discovered to date. Thanks to the best X-ray coverage spanning over 20 years with the deepest total exposure of ~ 9.5 Ms, its relatively well-sampled and long-timescale light curves enabled testing of existing TDE models. A TDE by a single SMBH or a pTDE scenario cannot explain the primary trend of the XID 935 light curves. In contrast, the SMBHB TDE model successfully reproduces the overall behavior of the light curves; however, it still fails to match short-timescale fluctuations exactly. Therefore, the exceptional observational features of XID 935 provide a key benchmark for refining quantitative TDE models and simulations. Ongoing time-domain X-ray surveys conducted by facilities like the Einstein Probe [85,86] may significantly enlarge the sample of X-ray TDEs, alongside XID 935, further enriching our knowledge of TDEs and their underlying physics.

RESOURCE AVAILABILITY

Materials availability

This study did not generate new unique materials/reagents.

Data and code availability

Raw data for the observations taken with Chandra, XMM-Newton, ROSAT, and Swift are available through the HEASARC online archive services: https://heasarc.gsfc.nasa.gov/docs/archive.html. The authors can provide other data supporting the findings of this study on request.

FUNDING AND ACKNOWLEDGMENTS

Many thanks to W. N. Brandt for his valuable comments on this manuscript. This work is supported by the National Key R&D Program of China (2023YFA1608100 and 2022YFF0503401), NSFC grants (12025303 and 12393814), and the Strategic Priority Research Program of the Chinese Academy of Sciences (XDB0550300). S.L. acknowledges the support by the National Science Foundation of China under grant NSFC No. 12473017. F.E.B. acknowledges support from ANID-Chile BASAL CATA FB210003, FONDECYT Regular 1241005, and Millennium Science Initiative Program – ICN12_009. J.-H.C. acknowledges the support from the National Natural Science Foundation of China (Grant No. 12503053). A.V.F.'s group at UC Berkeley received financial assistance from the Christopher R. Redlich Fund, as well as donations from Gary and Cynthia Bengier, Clark and Sharon Winslow, Alan Eustace and Kathy Kwan, William Draper, Timothy and Melissa Draper, Briggs and Kathleen Wood, Sanford Robertson (W.Z. is a Bengier-Winslow-Eustace Specialist in Astronomy, T.G.B. is a Draper-Wood-Robertson Specialist in Astronomy, Y.Y. was a Bengier-Winslow-Robertson Fellow in Astronomy), and numerous other donors. The W. M. Keck Observatory is operated as a scientific partnership among the California Institute of Technology, the University of California, and NASA; the observatory was made possible by the generous financial support of the W. M. Keck Foundation. The funders had no role in study design, data collection and analysis, decision to publish, or preparation of the manuscript.

AUTHOR CONTRIBUTIONS

Y.X. designed the project. M.H. analyzed the Chandra, XMM-Newton, and Swift data, and performed SED fitting. M.H. and Y.X. wrote the manuscript. S.L. and F.L. constructed the SMBHB TDE model. J.-H.C. and R.-F.S. constructed the pTDE model. Y.Y., A.V.F., W.Z., and T.G.B. obtained the new Keck/LRIS optical spectrum. Y.W. analyzed the Keck/LRIS optical spectrum. All authors contributed to the manuscript and approved the final version.

DECLARATION OF INTERESTS

Yongguan Xue is a member of The Innovation's scientific advisory board and was blinded from

reviewing or making final decisions on the manuscript. Peer review was handled independently

of this member and their research group. The other authors declare no conflicts of interest.

SUPPLEMENTAL INFORMATION

Supplemental information includes eight figures, one listing, and six tables.

LEAD CONTACT WEBSITE

Menggiu Huang: https://orcid.org/0009-0003-5280-0755

Yongguan Xue: https://orcid.org/0000-0002-1935-8104

References

[1] M. Schmidt. (1963). 3C 273: A Star-Like Object with Large Red-Shift. *Nature* **197**(4872):

1040. DOI: 10.1038/1971040a0.

[2] J. G. Hills. (1975). Possible power source of Seyfert galaxies and QSOs. *Nature* **254**(5498):

295-298. DOI: 10.1038/254295a0.

[3] P. J. Young, G. A. Shields and J. C. Wheeler. (1977). The black tide model of QSOs.. Astro-

phys. J. 212: 367-382. DOI: 10.1086/155056.

[4] J. Frank. (1978). Tidal disruption by a massive black hole and collisions in galactic nuclei...

Mon. Not. Roy. Astron. Soc. 184: 87-99. DOI: 10.1093/mnras/184.1.87.

[5] J. Magorrian and S. Tremaine. (1999). Rates of tidal disruption of stars by massive cen-

tral black holes. Mon. Not. Roy. Astron. Soc. 309(2): 447-460. DOI: 10.1046/j.1365-

8711.1999.02853.x.

22

- [6] X. Zhang, Y. Lu and Z. Liu. (2019). Effect of Accreting Tidally Disrupted Stars on the Spin Evolution of $\sim \! 10^6$ M $_\odot$ Black Holes. *Astrophys. J.* **877**(2): 143. DOI: 10.3847/1538-4357/ab1d48.
- [7] K. Zubovas. (2019). Tidal disruption events can power the observed AGN in dwarf galaxies. *Mon. Not. Roy. Astron. Soc.* **483**(2): 1957–1969. DOI: 10.1093/mnras/sty3211.
- [8] L. Ferrarese and H. Ford. (2005). Supermassive Black Holes in Galactic Nuclei: Past, Present and Future Research. Space Sci. Rev 116(3-4): 523–624. DOI: 10.1007/s11214-005-3947-6.
- [9] H. Netzer. (2015). Revisiting the Unified Model of Active Galactic Nuclei. Ann. Rev. Astron. Astrophys. 53: 365–408. DOI: 10.1146/annurev-astro-082214-122302.
- [10] M. J. Rees. (1988). Tidal disruption of stars by black holes of 10⁶-10⁸ solar masses in nearby galaxies. *Nature* **333**(6173): 523–528. DOI: 10.1038/333523a0.
- [11] S. Komossa and N. Bade. (1999). The giant X-ray outbursts in NGC 5905 and IC 3599: Follow-up observations and outburst scenarios. *Astron. Astrophys.* 343: 775–787. DOI: 10.48550/arXiv.astro-ph/9901141.
- [12] S. Sazonov, M. Gilfanov, P. Medvedev et al. (2021). First tidal disruption events discovered by SRG/eROSITA: X-ray/optical properties and X-ray luminosity function at z < 0.6. *Mon. Not. Roy. Astron. Soc.* 508(3): 3820–3847. DOI: 10.1093/mnras/stab2843.
- [13] E. Hammerstein, S. van Velzen, S. Gezari et al. (2023). The Final Season Reimagined: 30 Tidal Disruption Events from the ZTF-I Survey. *Astrophys. J.* 942(1): 9. DOI: 10.3847/1538-4357/aca283.
- [14] J. Guillochon and E. Ramirez-Ruiz. (2013). Hydrodynamical Simulations to Determine the Feeding Rate of Black Holes by the Tidal Disruption of Stars: The Importance of the Impact Parameter and Stellar Structure. *Astrophys. J.* 767(1): 25. DOI: 10.1088/0004-637X/767/1/25.
- [15] E. R. Coughlin and C. J. Nixon. (2019). Partial Stellar Disruption by a Supermassive Black

- Hole: Is the Light Curve Really Proportional to t $^{-9/4}$?. *Astrophys. J. Lett.* **883**(1): L17. DOI: 10.3847/2041-8213/ab412d.
- [16] E. S. Phinney. (1989). Manifestations of a Massive Black Hole in the Galactic Center. in:M. Morris (Ed.), The Center of the Galaxy. Vol. 136. 1989. p. 543.
- [17] T. Ryu, J. Krolik, T. Piran et al. (2020). Tidal Disruptions of Main-sequence Stars. III. Stellar Mass Dependence of the Character of Partial Disruptions. *Astrophys. J.* 904(2): 100. DOI: 10.3847/1538-4357/abb3ce.
- [18] D. N. Burrows, J. A. Kennea, G. Ghisellini et al. (2011). Relativistic jet activity from the tidal disruption of a star by a massive black hole. *Nature* **476**(7361): 421–424. DOI: 10.1038/nature10374.
- [19] F. K. Liu, S. Li and X. Chen. (2009). Interruption of Tidal-Disruption Flares by Supermassive Black Hole Binaries. *Astrophys. J. Lett.* 706(1): L133–L137. DOI: 10.1088/0004-637X/706/1/L133.
- [20] F. K. Liu, S. Li and S. Komossa. (2014). A Milliparsec Supermassive Black Hole Binary Candidate in the Galaxy SDSS J120136.02+300305.5. Astrophys. J. 786(2): 103. DOI: 10.1088/0004-637X/786/2/103.
- [21] X. Shu, W. Zhang, S. Li et al. (2020). X-ray flares from the stellar tidal disruption by a candidate supermassive black hole binary. *Nature Communications* **11**: 5876. DOI: 10.1038/s41467-020-19675-z.
- [22] R. Saxton, S. Komossa, K. Auchettl et al. (2020). X-Ray Properties of TDEs. Space Sci. Rev 216(5): 85. DOI: 10.1007/s11214-020-00708-4.
- [23] I. Andreoni, M. W. Coughlin, D. A. Perley et al. (2022). A very luminous jet from the disruption of a star by a massive black hole. *Nature* 612(7940): 430–434. DOI: 10.1038/s41586-022-05465-8.
- [24] B. Luo, W. N. Brandt, Y. Q. Xue et al. (2017). The Chandra Deep Field-South Survey: 7 Ms Source Catalogs. Astrophys. J., Suppl. Ser. 228(1): 2. DOI: 10.3847/1538-4365/228/1/2.

- [25] Y. Q. Xue. (2017). The Chandra deep fields: Lifting the veil on distant active galactic nuclei and X-ray emitting galaxies. New Astron. Rev 79: 59–84. DOI: 10.1016/j.newar.2017.09.002.
- [26] B. D. Lehmer, W. N. Brandt, D. M. Alexander et al. (2005). The Extended Chandra Deep Field-South Survey: Chandra Point-Source Catalogs. *Astrophys. J., Suppl. Ser.* 161(1): 21–40. DOI: 10.1086/444590.
- [27] Y. Q. Xue, B. Luo, W. N. Brandt et al. (2016). The 2 Ms Chandra Deep Field-North Survey and the 250 ks Extended Chandra Deep Field-South Survey: Improved Point-source Catalogs. *Astrophys. J., Suppl. Ser.* 224(2): 15. DOI: 10.3847/0067-0049/224/2/15.
- [28] P. Ranalli, A. Comastri, C. Vignali et al. (2013). The XMM deep survey in the CDF-S. III. Point source catalogue and number counts in the hard X-rays. Astron. Astrophys. 555: A42. DOI: 10.1051/0004-6361/201321211.
- [29] Q. Ni, W. N. Brandt, C.-T. Chen et al. (2021). The XMM-SERVS Survey: XMM-Newton Point-source Catalogs for the W-CDF-S and ELAIS-S1 Fields. *Astrophys. J., Suppl. Ser.* 256(1): 21. DOI: 10.3847/1538-4365/ac0dc6.
- [30] J. Truemper. (1982). The ROSAT mission. Advances in Space Research 2(4): 241–249.
 DOI: 10.1016/0273-1177(82)90070-9.
- [31] D. N. Burrows, J. E. Hill, J. A. Nousek et al. (2005). The Swift X-Ray Telescope. Space Sci. Rev 120(3-4): 165–195. DOI: 10.1007/s11214-005-5097-2.
- [32] A. Merloni, G. Lamer, T. Liu et al. (2024). The SRG/eROSITA all-sky survey. First X-ray catalogues and data release of the western Galactic hemisphere. *Astron. Astrophys.* 682: A34. DOI: 10.1051/0004-6361/202347165.
- [33] R. D. Cousins, J. T. Linnemann and J. Tucker. (2008). Evaluation of three methods for calculating statistical significance when incorporating a systematic uncertainty into a test of the background-only hypothesis for a Poisson process. *Nuclear Instruments and Methods* in Physics Research A 595(2): 480–501. DOI: 10.1016/j.nima.2008.07.086.

- [34] A. A. Stark, C. F. Gammie, R. W. Wilson et al. (1992). The Bell Laboratories H i Survey. Astrophys. J., Suppl. Ser. 79: 77. DOI: 10.1086/191645.
- [35] G. Vianello. (2018). Bias in profile poisson likelihood. *GitHub, https://giacomov.github.io/Bias-in-profile-poisson-likelihood/*.
- [36] L. Bradley, B. Sipőcz, T. Robitaille et al. (2023). astropy/photutils: 1.8.0 (zenodo). .
- [37] G. Yang, M. Boquien, W. N. Brandt et al. (2022). Fitting AGN/Galaxy X-Ray-to-radio SEDs with CIGALE and Improvement of the Code. *Astrophys. J.* 927(2): 192. DOI: 10.3847/1538-4357/ac4971.
- [38] M. Damen, I. Labbé, P. G. van Dokkum et al. (2011). The SIMPLE Survey: Observations, Reduction, and Catalog. *Astrophys. J.* **727**(1): 1. DOI: 10.1088/0004-637X/727/1/1.
- [39] D. Elbaz, M. Dickinson, H. S. Hwang et al. (2011). GOODS-Herschel: an infrared main sequence for star-forming galaxies. *Astron. Astrophys.* 533: A119. DOI: 10.1051/0004-6361/201117239.
- [40] B. Magnelli, D. Elbaz, R. R. Chary et al. (2011). Evolution of the dusty infrared luminosity function from z = 0 to z = 2.3 using observations from Spitzer. *Astron. Astrophys.* **528**: A35. DOI: 10.1051/0004-6361/200913941.
- [41] A. J. Barger, L. L. Cowie, F. E. Bauer et al. (2019). A Submillimeter Perspective on the GOODS Fields (SUPER GOODS). IV. The Submillimeter Properties of X-Ray Sources in the CDF-S. Astrophys. J. 887(1): 23. DOI: 10.3847/1538-4357/ab5116.
- [42] C. Y. Peng, L. C. Ho, C. D. Impey et al. (2002). Detailed Structural Decomposition of Galaxy Images. *Astron. J* **124**(1): 266–293. DOI: 10.1086/340952.
- [43] J. B. Oke, J. G. Cohen, M. Carr et al. (1995). The Keck Low-Resolution Imaging Spectrometer. *Publ. Astron. Soc. Pac.* **107**: 375. DOI: 10.1086/133562.
- [44] D. A. Perley. (2019). Fully Automated Reduction of Longslit Spectroscopy with the Low Resolution Imaging Spectrometer at the Keck Observatory. *Publ. Astron. Soc. Pac.* 131(1002): 084503. DOI: 10.1088/1538-3873/ab215d.

- [45] E. F. Schlafly and D. P. Finkbeiner. (2011). Measuring Reddening with Sloan Digital Sky Survey Stellar Spectra and Recalibrating SFD. *Astrophys. J.* 737(2): 103. DOI: 10.1088/0004-637X/737/2/103.
- [46] E. L. Fitzpatrick. (1999). Correcting for the Effects of Interstellar Extinction. *Publ. Astron. Soc. Pac.* **111**(755): 63–75. DOI: 10.1086/316293.
- [47] M. Cappellari and E. Emsellem. (2004). Parametric Recovery of Line-of-Sight Velocity Distributions from Absorption-Line Spectra of Galaxies via Penalized Likelihood. *Publ. Astron. Soc. Pac.* 116(816): 138–147. DOI: 10.1086/381875.
- [48] M. Cappellari. (2017). Improving the full spectrum fitting method: accurate convolution with Gauss-Hermite functions. *Mon. Not. Roy. Astron. Soc.* **466**(1): 798–811. DOI: 10.1093/mn-ras/stw3020.
- [49] Y. Avni. (1976). Energy spectra of X-ray clusters of galaxies.. Astrophys. J. 210: 642–646.
 DOI: 10.1086/154870.
- [50] D. E. Vanden Berk, G. T. Richards, A. Bauer et al. (2001). Composite Quasar Spectra from the Sloan Digital Sky Survey. Astron. J 122(2): 549–564. DOI: 10.1086/321167.
- [51] C. R. Evans and C. S. Kochanek. (1989). The Tidal Disruption of a Star by a Massive Black Hole. *Astrophys. J. Lett.* **346**: L13. DOI: 10.1086/185567.
- [52] R. Giacconi, A. Zirm, J. Wang et al. (2002). Chandra Deep Field South: The 1 Ms Catalog.
 Astrophys. J., Suppl. Ser. 139(2): 369–410. DOI: 10.1086/338927.
- [53] G. P. Szokoly, J. Bergeron, G. Hasinger et al. (2004). The Chandra Deep Field-South: Optical Spectroscopy. I.. Astrophys. J., Suppl. Ser. 155(2): 271–349. DOI: 10.1086/424707.
- [54] X. C. Zheng, Y. Q. Xue, W. N. Brandt et al. (2017). Deepest View of AGN X-Ray Variability with the 7 Ms Chandra Deep Field-South Survey. *Astrophys. J.* 849(2): 127. DOI: 10.3847/1538-4357/aa9378.
- [55] F. E. Bauer, E. Treister, K. Schawinski et al. (2017). A new, faint population of X-ray transients. *Mon. Not. Roy. Astron. Soc.* **467**(4): 4841–4857. DOI: 10.1093/mnras/stx417.

- [56] Y. Q. Xue, X. C. Zheng, Y. Li et al. (2019). A magnetar-powered X-ray transient as the aftermath of a binary neutron-star merger. *Nature* 568(7751): 198–201. DOI: 10.1038/s41586-019-1079-5.
- [57] L.-M. Yu, B. Luo, W. N. Brandt et al. (2023). X-Ray Unveiling Events in a $z\approx 1.6$ Active Galactic Nucleus in the 7 Ms Chandra Deep Field-South. *Astrophys. J.* **949**(1): 6. DOI: 10.3847/1538-4357/acc17e.
- [58] T. M. O. Franzen, E. M. Sadler, R. Chhetri et al. (2014). Deep 20-GHz survey of the Chandra Deep Field South and SDSS Stripe 82: source catalogue and spectral properties. *Mon. Not. Roy. Astron. Soc.* 439(2): 1212–1230. DOI: 10.1093/mnras/stt2322.
- [59] M. T. Huynh, A. M. Hopkins, E. Lenc et al. (2012). The ATLAS 5.5 GHz survey of the extended Chandra Deep Field South: catalogue, source counts and spectral indices. *Mon. Not. Roy. Astron. Soc.* 426(3): 2342–2358. DOI: 10.1111/j.1365-2966.2012.21894.x.
- [60] P. C. Zinn, E. Middelberg, R. P. Norris et al. (2012). The Australia Telescope Large Area Survey: 2.3 GHz observations of ELAIS-S1 and CDF-S. Spectral index properties of the faint radio sky. *Astron. Astrophys.* 544: A38. DOI: 10.1051/0004-6361/201219349.
- [61] N. A. Miller, E. B. Fomalont, K. I. Kellermann et al. (2008). The VLA 1.4 GHz Survey of the Extended Chandra Deep Field-South: First Data Release. *Astrophys. J., Suppl. Ser.* 179(1): 114–123. DOI: 10.1086/591054.
- [62] N. A. Miller, M. Bonzini, E. B. Fomalont et al. (2013). The Very Large Array 1.4 GHz Survey of the Extended Chandra Deep Field South: Second Data Release. *Astrophys. J., Suppl. Ser.* 205(2): 13. DOI: 10.1088/0067-0049/205/2/13.
- [63] R. P. Norris, J. Afonso, P. N. Appleton et al. (2006). Deep ATLAS Radio Observations of the Chandra Deep Field-South/Spitzer Wide-Area Infrared Extragalactic Field. *Astron. J* 132(6): 2409–2423. DOI: 10.1086/508275.
- [64] C. A. Hales, R. P. Norris, B. M. Gaensler et al. (2014). ATLAS 1.4 GHz data release 2 II. Properties of the faint polarized sky. *Mon. Not. Roy. Astron. Soc.* 440(4): 3113–3139. DOI: 10.1093/mnras/stu500.

- [65] J. J. Condon, W. D. Cotton, E. W. Greisen et al. (1998). The NRAO VLA Sky Survey. Astron. J 115(5): 1693–1716. DOI: 10.1086/300337.
- [66] J. Afonso, H. Messias, B. Mobasher et al. (2007). Deep ATCA and GMRT Observations of the CDFS. in: J. Afonso, H. C. Ferguson, B. Mobasher et al (Eds.), Deepest Astronomical Surveys. Vol. 380 of Astronomical Society of the Pacific Conference Series. 2007. p. 243.
- [67] R. B. Wayth, E. Lenc, M. E. Bell et al. (2015). GLEAM: The GaLactic and Extragalactic All-Sky MWA Survey. *Publ. Astron. Soc. Aust* **32**: e025. DOI: 10.1017/pasa.2015.26.
- [68] N. Hurley-Walker, J. Morgan, R. B. Wayth et al. (2014). The Murchison Widefield Array Commissioning Survey: A Low-Frequency Catalogue of 14 110 Compact Radio Sources over 6 100 Square Degrees. *Publ. Astron. Soc. Aust* 31: e045. DOI: 10.1017/pasa.2014.40.
- [69] A. S. Cohen, W. M. Lane, W. D. Cotton et al. (2007). The VLA Low-Frequency Sky Survey.
 Astron. J 134(3): 1245–1262. DOI: 10.1086/520719.
- [70] K. I. Kellermann, E. B. Fomalont, V. Mainieri et al. (2008). The VLA Survey of the Chandra Deep Field-South. I. Overview and the Radio Data. *Astrophys. J., Suppl. Ser.* 179(1): 71–94. DOI: 10.1086/591055.
- [71] H. B. Gim, M. S. Yun, F. N. Owen et al. (2019). Nature of Faint Radio Sources in GOODS-North and GOODS-South Fields. I. Spectral Index and Radio-FIR Correlation. *Astrophys. J.* 875(2): 80. DOI: 10.3847/1538-4357/ab1011.
- [72] S. Alberts, W. Rujopakarn, G. H. Rieke et al. (2020). Completing the Census of AGN in GOODS-S/HUDF: New Ultradeep Radio Imaging and Predictions for JWST. *Astrophys. J.* 901(2): 168. DOI: 10.3847/1538-4357/abb1a0.
- [73] M. Lacy, S. A. Baum, C. J. Chandler et al. (2020). The Karl G. Jansky Very Large Array Sky Survey (VLASS). Science Case and Survey Design. *Publ. Astron. Soc. Pac.* 132(1009): 035001. DOI: 10.1088/1538-3873/ab63eb.
- [74] I. Balestra, V. Mainieri, P. Popesso et al. (2010). The Great Observatories Origins Deep Survey. VLT/VIMOS spectroscopy in the GOODS-south field: Part II. Astron. Astrophys. 512: A12. DOI: 10.1051/0004-6361/200913626.

- [75] J. R. Trump, C. D. Impey, Y. Taniguchi et al. (2009). The Nature of Optically Dull Active Galactic Nuclei in COSMOS. *Astrophys. J.* 706(1): 797–809. DOI: 10.1088/0004-637X/706/1/797.
- [76] B. D. Lehmer, A. R. Basu-Zych, S. Mineo et al. (2016). The Evolution of Normal Galaxy X-Ray Emission through Cosmic History: Constraints from the 6 MS Chandra Deep Field-South. *Astrophys. J.* 825(1): 7. DOI: 10.3847/0004-637X/825/1/7.
- [77] S. A. Farrell, N. A. Webb, D. Barret et al. (2009). An intermediate-mass black hole of over 500 solar masses in the galaxy ESO243-49. *Nature* 460(7251): 73–75. DOI: 10.1038/nature08083.
- [78] R. C. E. van den Bosch. (2016). Unification of the fundamental plane and Super Massive Black Hole Masses. *Astrophys. J.* **831**(2): 134. DOI: 10.3847/0004-637X/831/2/134.
- [79] S. Gezari. (2021). Tidal Disruption Events. Ann. Rev. Astron. Astrophys. 59: 21–58. DOI: 10.1146/annurev-astro-111720-030029.
- [80] I. Timlin, John D., W. N. Brandt, S. Zhu et al. (2020). The frequency of extreme X-ray variability for radio-quiet quasars. *Mon. Not. Roy. Astron. Soc.* **498**(3): 4033–4050. DOI: 10.1093/mnras/staa2661.
- [81] L. Dai, J. C. McKinney and M. C. Miller. (2015). Soft x-ray temperature tidal disruption events from stars on deep plunging orbits. *ApJL* **812**: L39. DOI: 10.1088/2041-8205/812/2/l39.
- [82] C. Bonnerot, E. M. Rossi and G. Lodato. (2017). Long-term stream evolution in tidal disruption events. *MNRAS* **464**(3): 2816–2830. number: 3. DOI: 10.1093/mnras/stw2547.
- [83] J.-H. Chen and R.-F. Shen. (2021). Light Curves of Partial Tidal Disruption Events. Astrophys. J. 914(1): 69. DOI: 10.3847/1538-4357/abf9a7.
- [84] C. Bonnerot, W. Lu and P. F. Hopkins. (2021). First light from tidal disruption events. *MN-RAS*DOI: 10.1093/mnras/stab398.
- [85] W. Yuan, C. Zhang, Y. Chen et al. (2018). Einstein Probe: Exploring the ever-changing X-ray Universe. Scientia Sinica Physica, Mechanica & Astronomica 48(3): 039502. DOI: 10.1360/SSPMA2017-00297.

[86] C. C. Jin, D. Y. Li, N. Jiang et al. (2025). An Intermediate-mass Black Hole Lurking in A Galactic Halo Caught Alive during Outburst. arXiv e-prints: arXiv:2501.09580DOI: 10.48550/arXiv.2501.09580. Supplemental Information

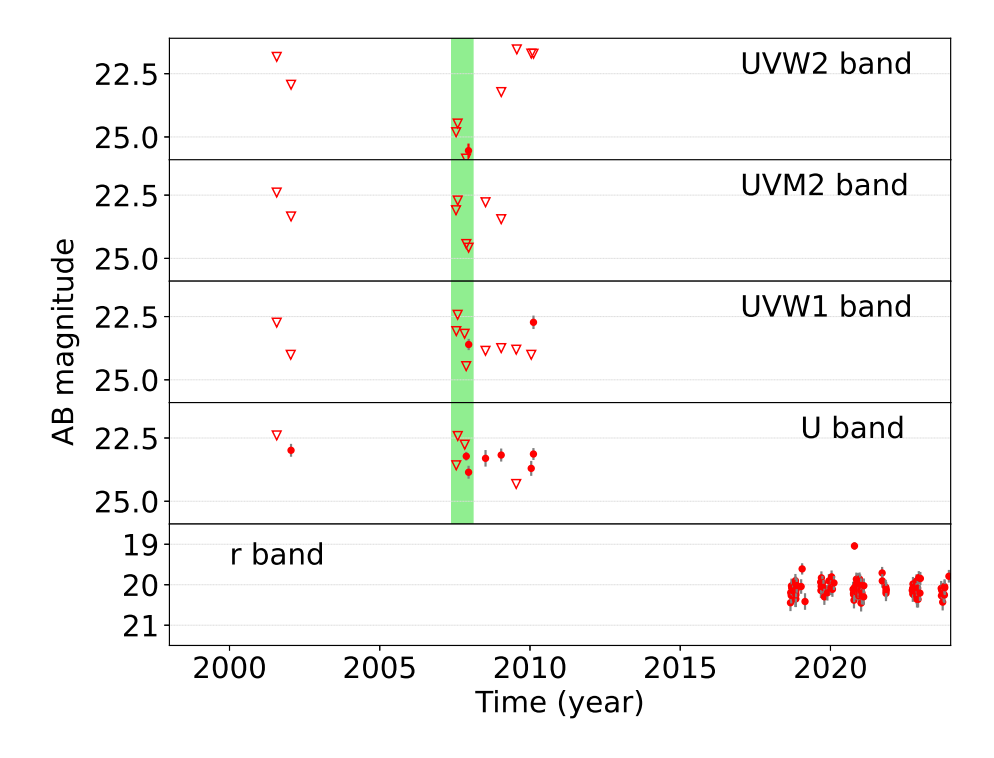


Figure S1: Optical/UV light curves of XID 935. From top to bottom, the bands are rest-frame UVW2, UVM2, UVW1, U, and r bands, respectively. For UVW2, UVM2, UVW1, and U bands, the Swift/UVOT data are green-shaded; outside the shaded region are the XMM-Newton/OM data. The r-band data are from the ZTF. Error bars correspond to $1\text{-}\sigma$ uncertainties. Triangles are 90%-confidence-level upper limits.

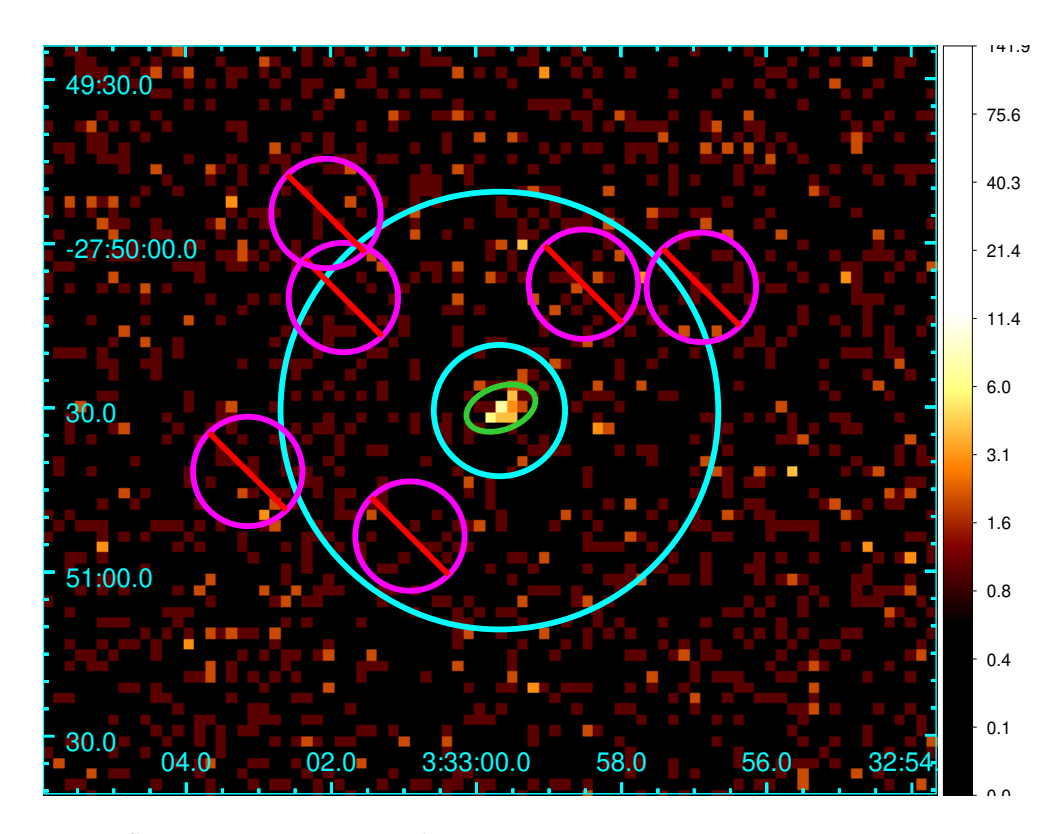


Figure S2: Extraction region for XID 935 in the CDF-S. The green ellipse is the source region. The cyan annulus is the background region, with 6 adjacent sources masked using magenta circles.

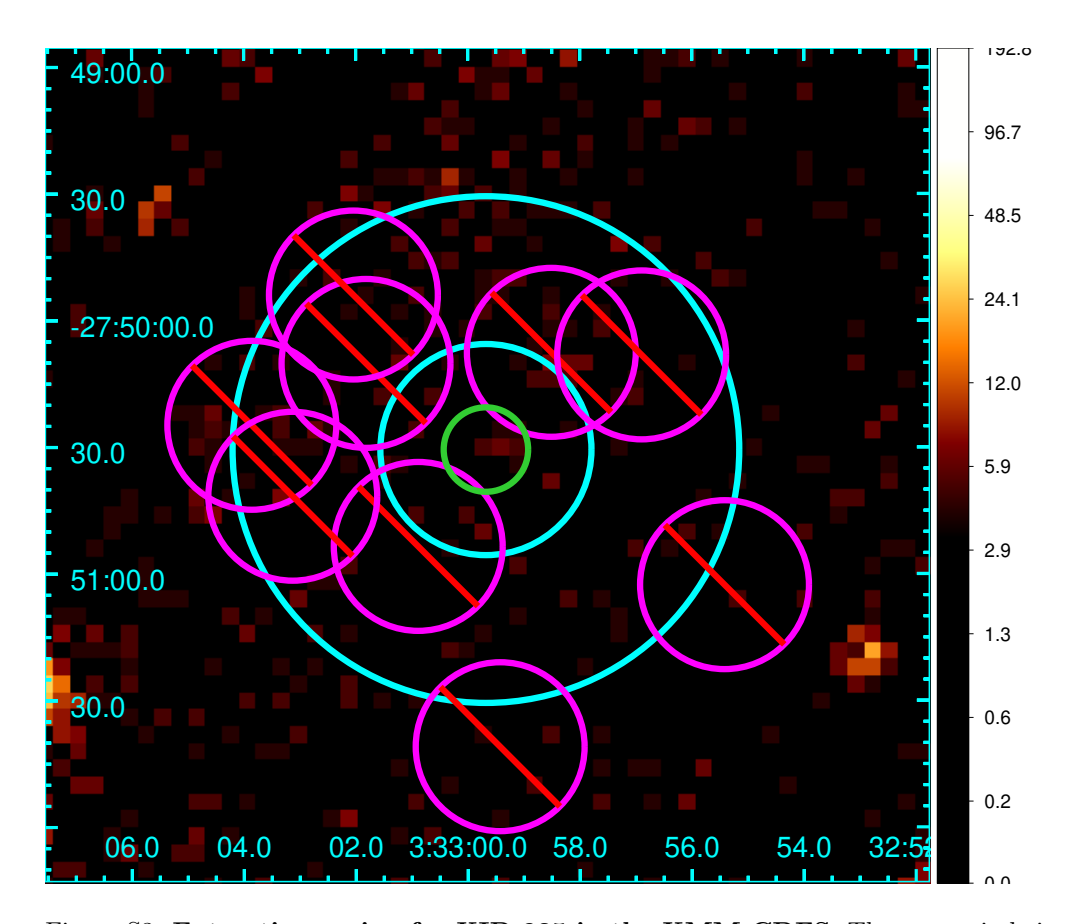


Figure S3: Extraction region for XID 935 in the XMM-CDFS. The green circle is the source region, and the cyan annulus is the background region, with 9 adjacent sources masked using magenta circles.

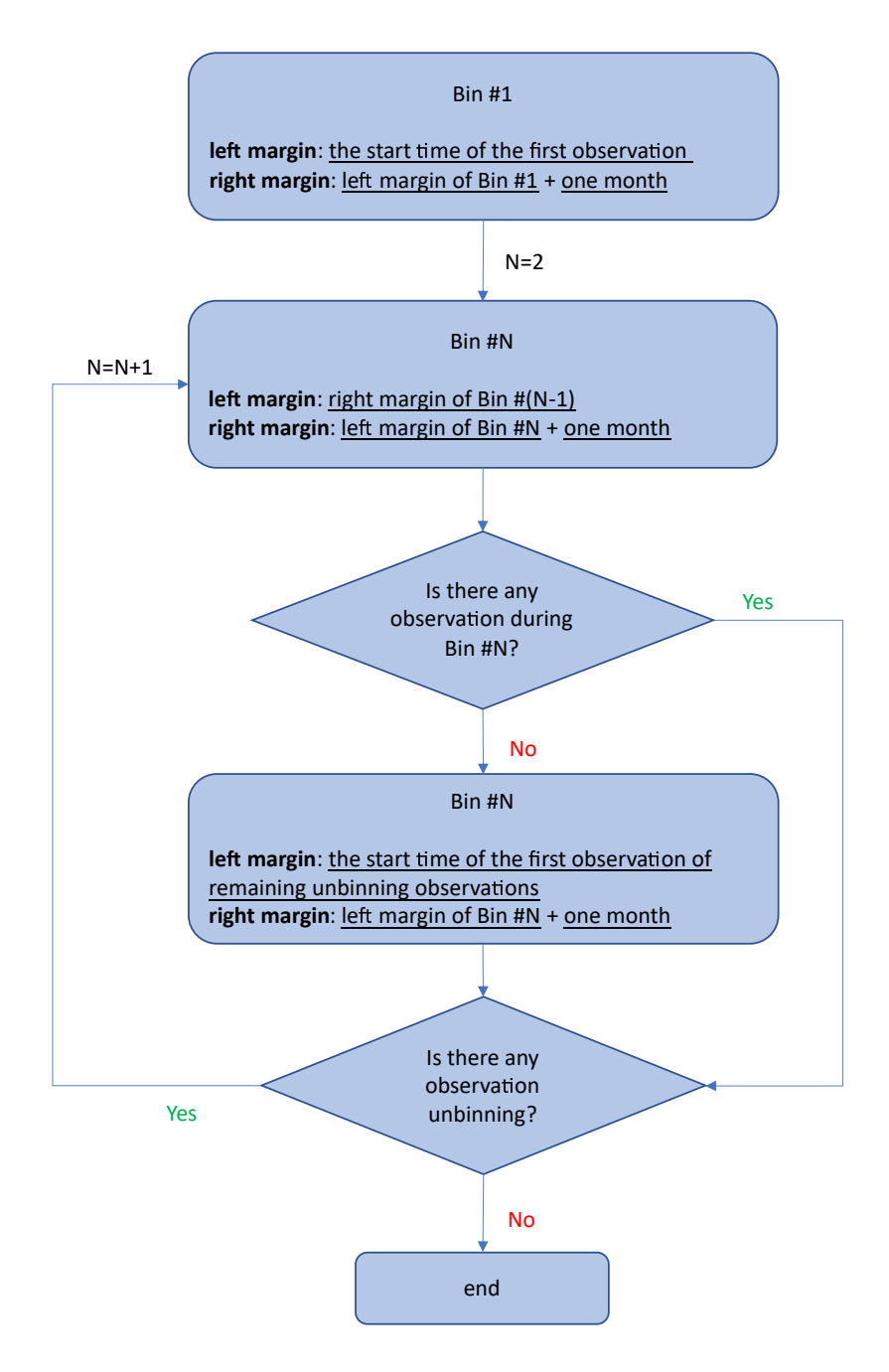


Figure S4: Month-bin flow diagram.

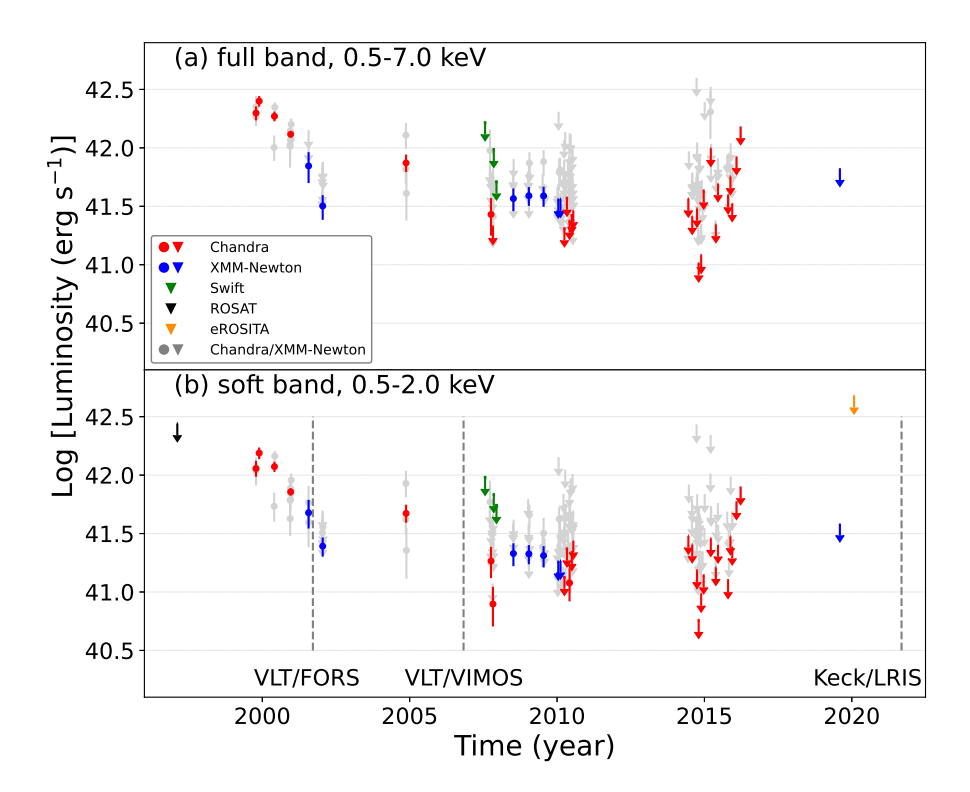


Figure S5: Month-bin X-ray light curves of XID 935. (a) Light curve in the rest-frame 0.5–7.0 keV band (full band, containing 768.9 ± 43.3 and 905.0 ± 84.0 Chandra and XMM-Newton net counts, respectively). (b) Light curve in the rest-frame 0.5–2.0 keV band (soft band, containing 595.9 ± 28.5 and 680.7 ± 62.6 Chandra and XMM-Newton net counts, respectively). Red, dark blue, green, black, and orange data are from Chandra, XMM-Newton, Swift, ROSAT, and eROSITA, respectively. Grey data represent individual observations of Chandra and XMM-Newton. Arrows indicate 90%-confidence-level upper limits. Dashed lines denote the observation times of optical spectra.

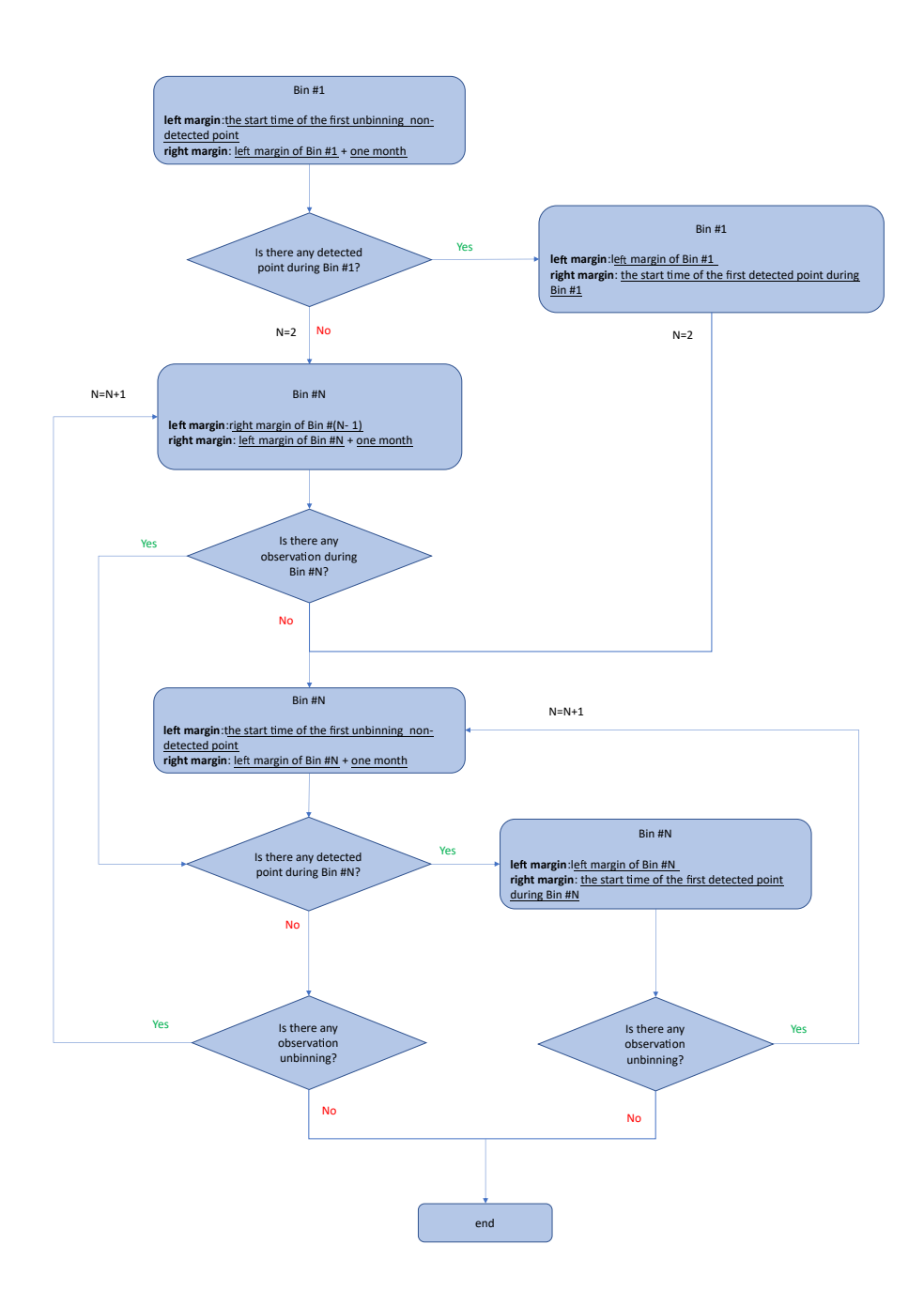


Figure S6: Adaptive-bin flow diagram.

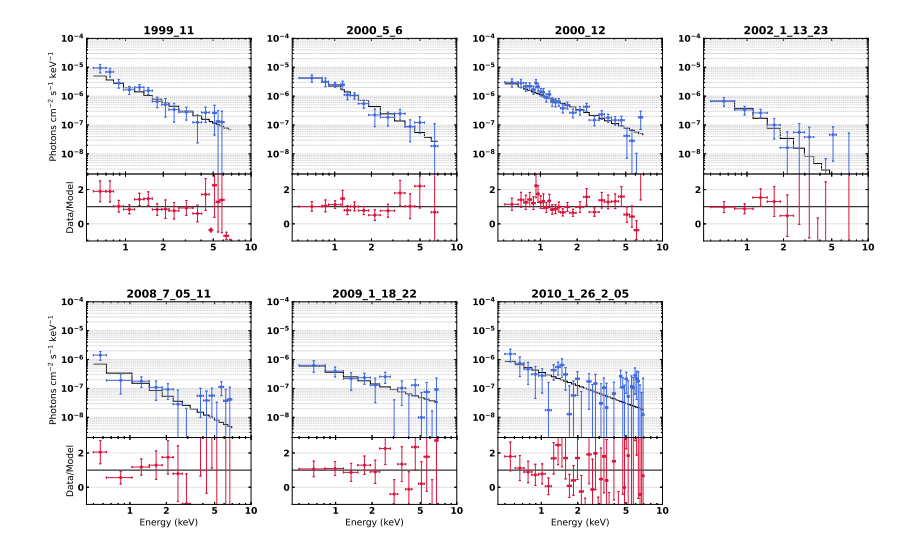


Figure S7: **X-ray spectra of XID 935.** Each panel displays the fitted spectrum and data-to-model ratio for time bins with net counts exceeding 60.

```
1 from scipy.special import xlogy # returns x * log(y), and return 0 if x=0 no matter y
 2 import numpy as np
 3 from scipy.stats import norm
 5 src_cts = value1 # total counts in source region
 6 bkg_cts = value2 # total counts in background region
 7 src_backscal = value3 # area of source region
 8 bkg_backscal = value4 # area of background region
10 def LRT(Src, Bkg, BkgScale=None):
    if BkgScale is None:
11
12
          try:
13
              net = Src - Bkg
14
              neglnLR = Bkg - Src + xlogy(Src, Src / Bkg)
15
         except ZeroDivisionError:
16
              return np.nan, np.nan
17
18
          net = Src - Bkg / BkgScale
19
         tot = Src + Bkg
20
         neglnLR = xlogy(Src, Src*(1 + BkgScale)/tot) + xlogy(Bkg, Bkg*(1 + BkgScale)/(BkgScale * tot))
21
22
     Z = np.where(net < 0, -np.sqrt(2 * neglnLR), np.sqrt(2 * neglnLR))</pre>
23
     return Z, norm.sf(Z)
24
25 Z, P_value = LRT(src_cts, bkg_cts, bkg_backscal / src_backscal)
26 print(Z) # Z in sigma units
27 print(P_value)
```

Listing S1: LRT Python code

Table S1: Chandra and XMM-Newton Observations

Observat	tion ID	Date	One-	month Bin	Adaptive Bin		
Chandra XMM-Newton			Total Exp.	Bin Name	Total Exp.	Bin Name	
			(ks)		(ks)		
581		1999/10/14	68.5	1999_10	68.5	1999_10	
1431-0		1999/10/15					
1431-1		1999/11/23	93.2	1999_11	93.2	1999_11	
441		2000/5/27	181.1	2000_5_6	181.1	2000_5_6	
582		2000/6/3					
2406		2000/12/10	631.4	2000 - 12	631.4	2000_12	
2405		2000/12/11					
2312		2000/12/13					
1672		2000/12/16					
2409		2000/12/19					
2313		2000/12/21					
2239		2000/12/23					
0	108060401	2001/7/27	33.2	$2001_{-}7$	33.2	2001_7	
0	108060501	2001/7/27					
0	108060601	2002/1/13	198.0	$2002_{-}1$	198.0	2002_1_13_23	
0	108060701	2002/1/14					
0	108061801	2002/1/16					
0	108061901	2002/1/17					
0	108062101	2002/1/20					
0	108062301	2002/1/23					
5021		2004/11/13	241.3	2004_11	241.3	2004_11	
5022		2004/11/15					
6164		2004/11/20					
8591		2007/9/20	359.8	2007_9_20_10_19	45.4	2007_9_20	
9593		2007/9/22			43.4	2007_9_22	
9718		2007/10/3			618.4	2007_10_03_30	
8593		2007/10/6					
8597		2007/10/17					
8595		2007/10/19					

		Table 51	Comminue	ed from previous pag	е	
8592		2007/10/22	600.1	2007_10_22_11_04		
8596		2007/10/24				
9575		2007/10/27				
9578		2007/10/30				
8594		2007/11/1			140.9	2007_11_01
9596		2007/11/4			111.8	2007_11_04
	0555780101	2008/7/5	378.9	2008_7	378.9	2008_7_05_11
	0555780201	2008/7/7				
	0555780301	2008/7/9				
	0555780401	2008/7/11				
	0555780501	2009/1/6	593.3	2009_1_06_24	313.3	2009_1_06_16
	0555780601	2009/1/10				
	0555780701	2009/1/12				
	0555780801	2009/1/16				
	0555780901	2009/1/18			184.5	2009_1_18_22
	0555781001	2009/1/22				
	0555782301	2009/1/24			95.5	2009_1_24
	0604960301	2009/7/5	375.0	2009_7_05_29	91.0	2009_7_05
	0604960201	2009/7/17			88.6	2009_7_17
	0604960101	2009/7/27			195.4	2009_7_27_29
	0604960401	2009/7/29				
	0604961101	2010/1/4	374.8	2010_1_04_26	283.5	2010_1_04_19
	0604961201	2010/1/8				
	0604960701	2010/1/12				
	0604960501	2010/1/18				
	0604961301	2010/1/19				
	0604960601	2010/1/26		•	172.9	2010_1_26_2_05
	0604960801	2010/2/5	329.9	2010_2_05_17		
	0604960901	2010/2/11			248.4	2010_2_11_17
	0604961001	2010/2/13				
	0604961801	2010/2/17				
12043		2010/3/18	694.0	2010_3_18_4_16	874.5	2010_3_18_5_17
12123		2010/3/21				
12044		2010/3/23				

	Table S1	continue	d from previous pag	ge	
12128	2010/3/27				
12045	2010/3/28				
12129	2010/4/3				
12135	2010/4/6				
12046	2010/4/8				
12047	2010/4/12				
12137	$2010/4/16$ _				
12138	2010/4/18	180.5	2010_4_18_5_17		
12055	2010/5/15				
12213	$2010/5/17$ _				
12048	2010/5/23	674.9	2010_5_23_6_15	674.9	2010_5_23_6_15
12049	2010/5/28				
12050	2010/6/3				
12222	2010/6/5				
12219	2010/6/6				
12051	2010/6/10				
12218	2010/6/11				
12223	2010/6/13				
12052	$2010/6/15$ _				
12220	2010/6/18	324.6	2010_6_18_7_16	406.6	2010_6_18_7_22
12053	2010/7/5				
12054	2010/7/9				
12230	2010/7/11				
12231	2010/7/12				
12227	2010/7/14				
12233	2010/7/16				
12232	2010/7/18	82.0	2010_7_18_22		
12234	2010/7/22 _				
16183	2014/6/9	144.8	2014_6_09_22	764.7	2014_6_09_10_08
16180	$2014/6/22$ _				
16456	2014/7/29	183.3	2014_7_29_8_06		
16641	2014/7/31				
16457	2014/8/5				
16644	2014/8/6				

	Table S1	l continu	ed from previous page	e	
16463	2014/9/23	312.7	2014_9_23_10_07		
17417	2014/9/25				
17416	2014/9/28				
16454	2014/10/1				
16176	2014/10/2				
16175	2014/10/3				
16178	2014/10/7				
16177	2014/10/8	706.6	2014_10_08_11_03		
16620	2014/10/10			1089.0	2014_10_10_2015_1_04
16462	2014/10/14				
17535	2014/10/17				
17542	2014/10/24				
16184	2014/10/26				
16182	2014/10/28				
16181	2014/10/31				
17546	2014/11/2				
16186	2014/11/2				
16187	2014/11/3 _				
16188	2014/11/13	390.5	2014_11_13_29		
16450	2014/11/18				
16190	2014/11/22				
16189	$2014/11/29_{-}$				
17556	2014/12/9	115.8	2014_12_09_2015_1_04		
16179	2014/12/31				
17573	2015/1/4 _				
17633	2015/3/16	226.2	2015_3_16_24	35.5	2015_3_16
17634	2015/3/19			991.3	2015_3_19_2016_3_24
16453	2015/3/21				
16451	2015/3/24 _				
16461	2015/5/19	210.8	2015_5_19_25		
16191	$2015/5/25$ _				
16460	2015/6/16	93.6	2015_6_16_20		
16459	2015/6/20 _				
17552	2015/10/10	231.4	2015_10_10_30		

		Table S1	continue	d from previous pag	ge	
16455		2015/10/27				
16458		2015/10/30				
17677		2015/11/15	125.1	2015_11_15_22		
18709		2015/11/22				
18719		2015/12/10	62.2	2015_12_10_12		
16452		2015/12/12				
18730		2016/2/2	29.1	2016_2_02		
16185		2016/3/24	48.4	2016_3_24		
	0827220901	2019/8/6	29.8	2019_8_06	29.8	2019_8_06

Table S2: ROSAT and Swift Observations

Observa	tion ID	Total Exp. (ks)	Bin Name
ROSAT	Swift	-	
RP190479N00		8.2	1997
RP190075N00			
RP190477N00			
	00037172001	41.5	2007_7_07_8_10
	00037172002		
	00037172003		
	00037172004		
	00037172005		
	00037172008		

00037172009		
00037172010		
00037172011		
00037172012		
00037172015		
00037172016		
00037172017		
00037172018		
00037172019		
00037172021		
00037172022		
00037172023		
00037172024		
00037172025		
00037172026		
00037172027		
00037172028		
00037172029		
00037172030		
00037172031		
00037172037	107.1	2007_10_25_11_23
00037172038		

00037172039		
00037172040		
00037172041		
00037172043		
00037172044		
00037172045		
00037172046		
00037172047		
00037172048		
00037172049		
00037172050		
00037172051		
00037172052		
00037172053		
00037172054		
00037172055		
00037172056		
00037172057		
00037172058		
00037172059		
00037172060		
00037172061	383.5	2007_11_24_29

Table S3: The detection results of various time bins

bin name	LRT	signifi	cance	n	et counts	1	zpow.index	ztbabs.nH
		σ						$10^{22}~{\rm cm}^{-2}$
	full	soft	hard	full	soft	hard	-	
	(1)	(2)	(3)	(4)	(5)	(6)	(7)	(8)
1999_10	14.78	14.21	6.02	$61.3^{+8.5}_{-8.4}$	$46.6^{+7.6}_{-7.0}$	$14.8^{+19.4}_{-10.8}$		
1999_11	19.74	19.86	6.67	$107.2^{+11.2}_{-11.1}$	$87.0_{-9.8}^{+9.9}$	$20.1_{-15.4}^{+25.6}$	$2.1_{-0.2}^{+0.2}$	< 0.086
2000_5_6	19.01	20.31	5.64	$131.1^{+12.6}_{-12.5}$	$108.0^{+11.1}_{-11.0}$	$23.1^{+29.4}_{-17.5}$	$2.5_{-0.4}^{+0.4}$	$0.16^{+0.16}_{-0.14}$
2000_12	28.23	27.09	12.34	$308.4^{+19.6}_{-19.4}$	$221.1^{+16.2}_{-16.0}$	$87.4^{+98.4}_{-76.4}$	$1.8_{-0.1}^{+0.1}$	< 0.075
2001_7	3.96	4.54	0.60	$42.1_{-12.1}^{+13.1}$	$38.3^{+11.0}_{-10.2}$	$3.8^{+9.8}_{-0.0}$		
$2002_1_13_23$	4.59	6.33	-0.22	$105.2^{+25.2}_{-25.0}$	$109.0^{+20.3}_{-20.1}$	$0.0^{+14.5}_{-0.0}$	$3.2^{+1.5}_{-0.9}$	$0.26^{+0.37}_{-0.24}$
2004_11	8.71	10.36	2.54	$48.7^{+8.8}_{-8.1}$	$38.5^{+7.2}_{-6.5}$	$10.2^{+15.5}_{-5.7}$		
2007_9_20	0.88	1.89	-0.32	$1.9_{-1.9}^{+2.4}$	$2.5^{+2.3}_{-1.6}$	$0.0^{+2.2}_{-0.0}$		
2007_9_22	3.04	3.81	0.91	$7.7_{-3.2}^{+3.9}$	$6.0^{+3.1}_{-2.4}$	$1.8^{+4.0}_{-0.0}$		
2007_10_03_30	1.56	3.40	-0.63	$11.4_{-7.0}^{+7.7}$	$15.1^{+5.9}_{-5.2}$	$0.0^{+5.0}_{-0.0}$		

,
١

	Ta	ble S3	conti	nued from	previous	page		
2007_11_01	3.22	2.98	1.85	$12.1_{-4.5}^{+5.2}$	$6.5^{+3.6}_{-2.8}$	$5.7^{+9.6}_{-2.4}$		
2007_11_04	1.03	0.79	0.72	$3.3^{+3.3}_{-2.8}$	$1.3^{+2.1}_{-1.3}$	$2.0_{-0.0}^{+4.7}$		
2008_7_05_11	4.81	4.89	1.65	$178.0^{+39.4}_{-39.1}$	$136.1^{+30.2}_{-30.1}$	$40.2^{+64.3}_{-17.1}$	$2.2^{+0.9}_{-0.4}$	< 0.32
2009_1_06_16	1.97	2.72	0.05	$55.6^{+28.2}_{-27.9}$	$54.9^{+21.2}_{-21.4}$	$0.9_{-0.0}^{+21.1}$		
$2009_1_18_22$	5.78	5.62	2.60	$131.4^{+25.6}_{-25.4}$	$89.4_{-18.6}^{+18.5}$	$42.2_{-25.2}^{+60.1}$	$1.2^{+0.6}_{-0.2}$	< 0.27
2009_1_24	2.73	1.87	1.98	$45.0^{+18.2}_{-17.3}$	$21.6^{+12.4}_{-11.6}$	$23.4_{-11.5}^{+36.4}$		
2009_7_05	2.67	3.37	0.36	$45.5_{-17.8}^{+18.7}$	$41.4^{+14.5}_{-13.4}$	$4.2^{+15.0}_{-0.0}$		
2009_7_17	4.37	3.25	2.93	$83.7^{+21.3}_{-21.1}$	$45.9^{+16.2}_{-15.3}$	$37.9^{+52.7}_{-24.0}$		
$2009_7_27_29$	2.69	2.83	1.01	$65.5^{+25.5}_{-25.4}$	$47.9^{+18.7}_{-17.8}$	$17.7^{+32.7}_{-3.4}$		
$2010_{-}1_{-}04_{-}19$	0.53	-0.50	1.25	$13.8^{+20.9}_{-13.8}$	$0.0_{-0.0}^{+15.2}$	$23.2^{+40.3}_{-6.9}$		
$2010_1_26_2_05$	5.47	5.79	1.92	$120.3_{-24.6}^{+24.6}$	$90.6^{+18.3}_{-18.5}$	$29.6_{-14.3}^{+45.9}$	$1.8^{+0.6}_{-0.5}$	< 0.12
$2010_{-}2_{-}11_{-}17$	0.93	0.98	0.34	$22.9_{-19.4}^{+20.2}$	$17.0^{+14.8}_{-14.0}$	$5.9_{-0.0}^{+21.6}$		
$2010_3_18_5_17$	2.06	3.00	0.40	$20.0^{+10.5}_{-9.8}$	$16.8^{+7.0}_{-6.3}$	$3.2^{+10.4}_{-0.0}$		
$2010_5_23_6_15$	1.99	3.94	-0.45	$16.8^{+9.3}_{-8.5}$	$19.8_{-6.0}^{+6.7}$	$0.0_{-0.0}^{+6.1}$		
$2010_6_18_7_22$	1.40	3.33	-0.85	$8.8^{+6.4}_{-5.9}$	$12.9_{-4.7}^{+5.3}$	$0.0^{+3.9}_{-0.0}$		

$2014_6_09_10_08$	1.75	3.42	-0.34	$12.8_{-7.3}^{+7.9}$	$14.8^{+5.8}_{-5.2}$	$0.0^{+5.7}_{-0.0}$
2014_10_10_2015_1_04	0.07	-0.27	0.25	$0.6^{+8.5}_{-0.6}$	$0.0_{-0.0}^{+4.5}$	$1.7^{+8.5}_{-0.0}$
2015_3_16	3.16	0.72	3.13	$7.4_{-3.1}^{+3.7}$	$0.6^{+1.6}_{-0.6}$	$6.8^{+10.3}_{-3.9}$
2015_3_19_2016_3_24	1.18	0.05	1.35	$9.9^{+7.9}_{-7.3}$	$0.2^{+5.0}_{-0.2}$	$9.7^{+16.8}_{-3.1}$
2019_8	-0.23	-0.11	-0.21	$0.0^{+7.2}_{-0.0}$	$0.0^{+5.5}_{-0.0}$	$0.0^{+5.6}_{-0.0}$

Table S4: Adaptive-bin Results

Bin Name	\mathbf{Time}	${ m Lumin_{0.5-7.0~keV}}$	$\operatorname{Lumin}_{0.5-2.0~\mathrm{keV}}$
	MJD	${\rm erg~s}^{-1}$	${\rm erg~s^{-1}}$
(1)	(2)	(3)	(4)
1997	50491.5 ± 5.0	none	< 42.44
1999_10	51466.5 ± 0.6	$42.30_{-0.06}^{+0.06}$	$42.06^{+0.07}_{-0.07}$
1999_11	51505.7 ± 0.6	$42.40^{+0.04}_{-0.05}$	$42.19_{-0.05}^{+0.05}$
2000_5_6	51695.4 ± 4.3	$42.27^{+0.04}_{-0.04}$	$42.07^{+0.04}_{-0.05}$
2000_12	51896.1 ± 7.1	$42.12^{+0.03}_{-0.03}$	$41.86^{+0.03}_{-0.03}$
$2001_{-}7$	52118.1 ± 0.6	$41.85^{+0.12}_{-0.15}$	$41.68^{+0.11}_{-0.13}$
2002_1_13_23	52292.8 ± 5.2	$41.50^{+0.09}_{-0.12}$	$41.39_{-0.09}^{+0.07}$
$2004_{-}11$	53326.4 ± 4.3	$41.87^{+0.07}_{-0.08}$	$41.67^{+0.07}_{-0.08}$
2007_7_07_8_10	54305.2 ± 16.5	< 42.22	< 41.98
2007_9_20	54363.5 ± 0.3	< 41.85	< 41.74
2007_9_22	54366.1 ± 0.3	$41.98^{+0.18}_{-0.24}$	$41.77^{+0.18}_{-0.23}$
2007_10_03_30	54390.5 ± 13.9	< 41.24	$40.95_{-0.19}^{+0.14}$
2007_11_01	54406.3 ± 0.8	$41.41^{+0.16}_{-0.20}$	< 41.33
2007_11_04	54408.8 ± 0.7	< 41.76	< 41.43
2007_10_25_11_23	54412.7 ± 14.6	< 41.99	< 41.83
2007_11_24_29	54446.4 ± 17.6	< 41.71	< 41.74
2008_7_05_11	54655.9 ± 3.7	$41.57^{+0.09}_{-0.11}$	$41.33_{-0.11}^{+0.09}$
2009_1_06_16	54843.5 ± 5.6	< 41.53	< 41.37

Table S4 continued from previous page

2009_1_18_22	54852.5 ± 2.7	$41.82^{+0.08}_{-0.09}$	$41.53_{-0.10}^{+0.08}$
2009_1_24	54856.5 ± 0.7	< 41.87	< 41.49
2009_7_05	55018.1 ± 0.7	< 41.77	$41.39_{-0.17}^{+0.13}$
2009_7_17	55030.0 ± 0.7	$41.88^{+0.10}_{-0.13}$	$41.50_{-0.18}^{+0.13}$
2009_7_27_29	55040.9 ± 1.8	< 41.62	< 41.37
2010_1_04_19	55208.5 ± 7.7	< 41.34	< 40.91
2010_1_26_2_05	55228.4 ± 5.7	$41.80^{+0.08}_{-0.10}$	$41.56^{+0.08}_{-0.10}$
2010_2_11_17	55242.4 ± 3.7	< 41.35	< 41.09
2010_3_18_5_17	55303.7 ± 30.6	< 41.33	$40.89_{-0.20}^{+0.15}$
2010_5_23_6_15	55351.6 ± 12.3	< 41.37	$41.08^{+0.13}_{-0.16}$
2010_6_18_7_22	55383.0 ± 17.4	< 41.33	$41.06_{-0.19}^{+0.15}$
2014_6_09_10_08	56879.0 ± 61.4	< 41.32	$41.01_{-0.19}^{+0.14}$
2014_10_10_2015_1_04	56983.6 ± 43.1	< 40.87	< 40.52
2015_3_16	57097.8 ± 0.2	$42.31_{-0.23}^{+0.18}$	< 42.01
2015_3_19_2016_3_24	57286.1 ± 185.9	< 41.26	< 40.80
2019_8	58701.8 ± 0.2	< 41.83	< 41.58

- 1. Column 1: name of the time bin.
- 2. Column 2: time of each time bin.
- 3. Column 3: 0.5–7.0 keV (rest-frame) luminosity. The value without error is 90% confidence level upper limit.
- 4. Column 4: same as Column 3, but for luminosity in 0.5-2.0 keV (rest-frame).

Table S5: One-month-bin Results

Bin Name	Time	$\operatorname{Lumin_{0.5-7.0~keV}}$	$\rm Lumin_{0.5-2.0~keV}$
	MJD	${\rm erg~s^{-1}}$	${\rm erg~s^{-1}}$
(1)	(2)	(3)	(4)
1997	50491.5±5.0	none	< 42.44
1999_10	51466.5 ± 0.6	$42.30_{-0.06}^{+0.06}$	$42.06^{+0.07}_{-0.07}$
1999_11	51505.7 ± 0.6	$42.40^{+0.04}_{-0.05}$	$42.19_{-0.05}^{+0.05}$
2000_5_6	51695.4 ± 4.3	$42.27^{+0.04}_{-0.04}$	$42.07^{+0.04}_{-0.05}$
2000_12	51896.1 ± 7.1	$42.12_{-0.03}^{+0.03}$	$41.86^{+0.03}_{-0.03}$
2001_7	52118.1 ± 0.6	$41.85_{-0.15}^{+0.12}$	$41.68^{+0.11}_{-0.13}$
$2002_{-}1$	52292.8 ± 5.2	$41.50_{-0.12}^{+0.09}$	$41.39^{+0.07}_{-0.09}$
2004_11	53326.4 ± 4.3	$41.87^{+0.07}_{-0.08}$	$41.67^{+0.07}_{-0.08}$
2007_7_07_8_10	54305.2 ± 16.5	< 42.22	< 41.98
2007_9_20_10_19	54378.6 ± 15.4	$41.43_{-0.18}^{+0.14}$	$41.26^{+0.12}_{-0.15}$
2007_10_22_11_04	54402.5 ± 7.0	< 41.33	$40.90^{+0.15}_{-0.19}$
2007_10_25_11_23	54412.7 ± 14.6	< 41.99	< 41.83
2007_11_24_29	54446.4 ± 17.6	< 41.71	< 41.74
$2008_{-}7$	54655.9 ± 3.7	$41.57_{-0.11}^{+0.09}$	$41.33^{+0.09}_{-0.11}$
2009_1_06_24	54847.6 ± 9.7	$41.59^{+0.07}_{-0.09}$	$41.33^{+0.07}_{-0.09}$
2009_7_05_29	55030.0 ± 12.7	$41.59^{+0.08}_{-0.09}$	$41.31^{+0.08}_{-0.10}$
2010_1_04_26	55212.5 ± 11.7	< 41.56	< 41.26
2010_2_05_17	55239.4 ± 6.7	< 41.56	< 41.27

Table S5 continued from previous page

$\begin{array}{cccccccccccccccccccccccccccccccccccc$	
$\begin{array}{cccccccccccccccccccccccccccccccccccc$	
$2010_6_18_7_16 \qquad 55379.7\pm14.2 \qquad <41.42 \qquad <41.34$ $2010_7_18_22 \qquad 55398.1\pm2.3 \qquad <41.46 \qquad <41.44$ $2014_6_09_22 \qquad 56824.3\pm6.7 \qquad <41.56 \qquad <41.48$	
$2010_7_18_22$ 55398.1 ± 2.3 <41.46 <41.44 $2014_6_09_22$ 56824.3 ± 6.7 <41.56 <41.48	
$2014_6_09_22$ 56824.3 ± 6.7 < 41.56 < 41.48	
2014 7 20 8 06 56871 0+4 0 < 41 42 < 41 41	
2014_1_20_000 00011.0±4.0 41.42 41.41	
$2014_{-9} - 23_{-10} - 07$ 56930.7 ± 7.7 < 41.48 < 41.18	
$2014_{-}10_{-}08_{-}11_{-}03$ 56951.8 ± 12.9 < 41.01 < 40.76	
$2014_{-}11_{-}13_{-}29$ 56982.7 ± 8.6 < 41.08 < 40.98	
$2014_{-}12_{-}09_{-}2015_{-}1_{-}04 57013.8 \pm 12.8 < 41.63 < 41.14$	
$2015_3_16_24$ 57102.4 ± 4.8 < 42.00 < 41.46	
$2015_5_19_25$ 57164.7 ± 3.6 < 41.34 < 41.21	
$2015_6_16_20$ 57191.7 ± 2.4 < 41.70 < 41.40	
$2015_10_10_30$ 57316.2 ± 10.9 < 41.59 < 41.10	
$2015_11_15_22$ 57345.4 ± 3.7 < 41.75 < 41.47	
$2015_12_10_12$ 57367.8 ± 1.5 < 41.53 < 41.39	
$2016_{-}2_{-}02$ 57420.6 ± 0.2 < 41.93 < 41.78	
2016_3_24 57471.7 ± 0.3 < 42.18 < 41.90	
2019_8_06 58701.8 ± 0.2 <41.83 <41.58	

Table S6: Model Parameters for SED Fitting with CIGALE

Table 50. Hodel I arameter for 522 I forms with croff22				
Module	Parameter	Values		
Star-formation history SFR $\propto (t - T_0) exp(-\frac{t - T_0}{\tau})$	Stellar e-folding time	0.1, 0.2, 0.3, 0.4, 0.5, 0.6, 0.7, 0.8, 0.9,		
•		1, 2, 3, 4, 5, 6, 7, 8, 9, 10 Gyr		
	Stellar age	0.1, 0.2, 0.3, 0.4, 0.5, 0.6, 0.7, 0.8, 0.9,		
		1, 2, 3, 4, 5, 6, 7, 8, 9, 10 Gyr		
Simple stellar population	Initial mass function	Chabrier		
	Metallicity	0.0001, 0.0004, 0.004, 0.008, 0.02, 0.05		
Dust attenuation	$E(B-V)_{line}$	0, 0.05, 0.1, 0.15, 0.2, 0.25, 0.3, 0.4, 0.5,		
		0.6, 0.7, 0.8, 0.9, 1, 1.2, 1.5		
Galactic dust emission	Slope in $dU/dM \propto U^{\alpha}$	1.0, 1.5, 2.0, 2.5, 3.0		

Note. For parameters not listed here, we use the default values.